UNIVERSITÄT
DUISBURG
ESSEN

Open-Minded

Master Thesis

Magnetic Characterization of Organically Formed Magnetite Nanoparticle Arrangements in Magnetospirillum Gryphiswaldense

Alexandra Terwey - 2241662

Faculty of Physics
AG Farle
University Duisburg-Essen

Duisburg, December 2015

Abstract

This work focusses on the magnetic characterization of bio genetically formed iron oxide nanoparticle chains, with a particle size falling within a size range of $(20-30\,\mathrm{nm})^3$, inside of magnetotactic bacteria. The magnetite particles originate in wild type and mutant strains of the magnetotactic bacterium *Magnetospirillum Gryphiswaldense*. Mutations in *Magnetospirillum Gryphiswaldense* lead to different geometrical nanoparticle arrangements which have been characterized by ferromagnetic resonance (FMR) measurements. It was possible to distinguish different spin excitations in the nanoparticle chains within a single bacterium. The magnetic anisotropy energy density of single particles and the dipolar coupled excitations between particle arrangements could be observed and have been compared with micromagnetic simulations. The average demagnetization fields in between particles could be quantified with field values in a range of $50-70\,\mathrm{mT}$. At X-band frequencies the typical resonance of a single particle linewidth is $3\pm0.5\,\mathrm{mT}$. This value is five times smaller than the value for an epitaxial thin film of the same material. The crystalline anisotropy field $2K_4/M = 58\pm6\,\mathrm{mT}$ for the different single particles is in the same order of magnitude as bulk magnetite.

Kurzfassung

Diese Arbeit befasst sich mit der Charakterisierung von biologisch erzeugten Eisenoxid Nanopartikelketten, bestehend aus kuboktaedrischen Einzelpartikeln in einem Größenbereich von $(20-30\,\mathrm{nm})^3$. Diese Ketten befinden sich innerhalb von magnetotaktischen Bakterien. Hier wurden Zellen des natürlichen Wildtyps der Art *Magnetospirillum Gryphiswaldense* mit geraden Ketten untersucht, sowie Mutanten mit gestörter Kettenanordnung. Durch Mutationen der Bakterien können unterschiedliche geometrische Anordnungen der Nanopartikelketten gebildet werden, welche mit ferromagnetischen Resonanz Messungen (FMR) magnetisch charakterisiert wurden. Im Rahmen dieser Arbeit war es möglich unterschiedliche Spinanregungen in einer einzelnen Kette an einem einzelnen Bakterium zu beobachten. Die magnetische Anisotropie und dipolar gekoppelte Anregungen zwischen den Partikeln konnte experimentell beobachtet und mit mikromagnetischen Simulationen verglichen werden. Die Stärke der Entmagnetisierungsfelder zwischen den Partikeln konnte durch Simulationen auf einen Wertebereich von $50-70\,\mathrm{mT}$ quantifiziert werden. Bei X-Band Frequenzen kann eine Linienbreite von $3\pm0.5\,\mathrm{mT}$ für ein einzelnes Partikel extrahiert werden. Dieser Wert für ein einzelnes einkristallines Partikel ist fünf mal kleiner, als der Wert für epitaktisch gewachsene Magnetit Dünnfilme. Das magnetokristalline Anisotropiefeld hat einen Wert von $2K_4/M = 58\pm6\,\mathrm{mT}$ und befindet sich damit in der Größenordnung von Bulk-Magnetit.

Symbols

A - Exchange Constant

α - Gilbert Damping Factor

α_i - Directional Cosine

B_{res} - Resonance Field

$\vec{B}_{\mathrm{eff}}$ - Effective Magnetic Field

$\vec{B}_{\mathrm{ext}}$ - External Magnetic Field

$\vec{B}_{\mathrm{int}}$ - Internal Magnetic Field

b_1 - Perpendicular hf Field Component

$\vec{B}_{\mathrm{hf}}$ - Magnetic hf Component

$\vec{B}_{\mathrm{PP}}$ - Line Width

χ - Spin Wave Function

$\underline{\underline{\chi}}$ - High Frequency Susceptibility

$\vec{D}$ - angular momentum

$\vec{E}_{\mathrm{hf}}$ - Electric hf Component

E_{d} - Demagnetization Energy

F_{cub} - Cubic Anisotropy

F_{A} - Complete Anisotropy

F_{M_i} - Free Energy Density

F_{zeeman} - Zeeman Energy

F_{crystal} - Crystalline Anisotropy

F_{shape} - Shape Anisotropy

F_{surface} - Surface Anisotropy

f - Frequency

g - g Factor

g_{eff} - Effective g Factor

γ - Gyromagnetic Ratio

$\hbar$ - Reduced Planck's Constant

$\vec{H}_d$ - Demagnetization Field

H_{ex} - Exchange Interaction

J_{ij} - Exchange Integral

$\vec{j}$ - Complete Angular Momentum

$\vec{k}$ - Wave Vector

K_i - Anisotropy Constant

$\vec{l}$ - Angular Momentum

$\vec{l_{\mathrm{ex}}}$ - Exchange Length

$\vec{M}$ - Magnetization

$\vec{M}_{\mathrm{s}}$ - Saturation Magnetization

$\vec{\mu_i}$ - Magnetic Moment

μ_B - Bohr's Magneton

μ_0 - Magnetic Permeability

$\underline{\underline{N}}$ - Demagnetization Tensor

ω - Frequency

ω_L - Lamor Frequency

Φ - Spatial Wave Function

φ - In-Plane Angle

Ψ - Complete Wave Function

r - Distance

$\vec{S}_i$ - Spin

T_{C} - Curie Temperature

θ - Out-Of-Plane Angle

T_{V} - Verwey Temperature

Abbreviations

AFC - Automatic Frequency Control

DPPH - Di(phenyl)-(2,4,6-trinitrophenyl)iminoazanium

EPR - Electron Paramagnetic Resonance

FIB - Focussed Ion Beam

FMR - Ferromagnetic Resonance

FFT - Fast Fourier Transformation

HEPES - 2-[4-(2-hydroxyethyl)piperazin-1-yl]ethanesulfonic Acid

LLG - Landau Lifshitz Gilbert Equation

MCA - Magnetocrystalline Anisotropy

microFMR - FMR in Microresonators

MSR-1 - *Magnetospirllum Gryphiswaldense*

MTB - Magnetotactic Bacteria

OOMMF - Object Oriented MicroMagnetic Framework

PMR - Planar Micro Resonator

SEM - Scanning Electron Microscope

TEM - Transmission Electron Microscope

Contents

1. Introduction

Magnetotactic bacteria have been a field of interest for both physics and biology since their first discovery [Bel63] [Bla75]. Not only the mechanism of motion of those bacteria, but also the material specific parameters of the intracellular magnetic nanoparticles have been studied. Since recent scientific research focuses on the behavior of nanoscaled magnetic materials, the bio genetically formed magnetite nanoparticles are of interest, as nanoparticles may have different behavior than bulk material due to their small size and surface to volume ratio. The nanoparticles inside the magnetotactic bacteria strains can be used in a variety of biomedical applications and medical treatments due to their good biocompatibility. Those applications include such as hyperthermia [Her06] or magnetic imaging [Lee15], drug delivery by functionalization [Mat07] [Zha06] or enzyme immobilization [Mat87] by making use of their ferrimagnetic behavior. Genetic modifications of the bacteria make it possible to research on differently arranged magnetite nanoparticles. So far, only studies on bulk material have been reported [Wei04] [Fis08] [Geh11b] [Geh11a] [Abr14]. To gain more knowledge on the intrinsic behavior of single magnetite particles, ferromagnetic resonance (FMR) is a potent method to determine the magnetic properties like anisotropy and damping. Yet, ferromagnetic resonance measurements on a single magnetotactic bacterium cell have not been performed. In this work a case study on the magnetotactic bacterium strain *Magnetospirillum Gryphiswaldense* (MSR-1 strain) from a statistical amount of bacteria to a single cell is shown. The magnetic properties and coupling mechanisms between the nanoparticles such as different occurring excitation modes in the chains have been studied and corresponding simulations have been performed to validate the experiments done.

The first part of this thesis gives an overview of the theoretical background from magnetic interactions, anisotropies, to magnetite itself. The next part describes magnetotactic bacteria and their ability to bio genetically form magnetite crystals and how genetic mutation influences the arrangement of the nanoparticle chains, the size and the nanoparticle shape. The bacteria serve as a perfect naturally occurring model for a

coupled nanoparticle system with various geometrical arrangements. In this work only the magnetic properties of the particles are of interest. In the experimental part of this thesis first measurements on bulk samples will be discussed. It will be followed by the magnetic characterization of a downscaled system of bacteria cells, from 40 cells to a single cell with only one chain of magnetite nanoparticles. The experiments are then compared with micromagnetic simulations to extract the magnetocrystalline anisotropy of single magnetite particles and the dipolar interactions between the nanoparticles arranged in chain structures. In the end a conclusion and an outlook for further research will be given.

Comment: Throughout this work the magnetic flux $B = \mu_0 \cdot H$ is given as B-field. If not mentioned otherwise all used units are given as SI-units or are derived from them.

2. Theoretical Background

In this work the static and dynamic behavior of coupled ferrimagnetic nanoparticles has been studied. In order to understand the intrinsic magnetic mechanisms an overview of the theoretical background has to be given. To explain the origin of ferro-, respectively ferri-, magnetism, chapter 2.1 gives an overview on exchange coupling. To understand the magnetic anisotropies chapter 2.2 will introduce spin orbit coupling as a source for intrinsic anisotropies. Chapter 2.3 describes the g-factor, which gives the relation between spin and orbital momentum in a ferromagnet. As we study a sample system with linear nanoparticle chains, dipolar coupling strongly contributes and the demagnetization effect will be discussed in chapter 2.4. To determine the static and dynamic magnetization behavior the experimental methods electron paramagnetic resonance (EPR) and ferromagnetic resonance (FMR) have been used. Chapter 2.5 and 2.6 introduce the theoretical background for those techniques, connecting the measurement technique with the physical properties that can be extracted. Experimentally the sample system shows collective magnetic excitations, which will be introduced in chapter 2.8. In the last part of the theoretical overview, chapter 2.9 will give an introduction to the structural and intrinsic properties of magnetite.

2.1. Exchange Coupling

Uncompensated magnetic moments in a magnetic material either align parallel (ferromagnetism), or antiparallel (ferri- or antiferromagnetism). This alignment can be explained quantum mechanically by the exchange interaction $\mathcal{H}_{\text{ex}}$.

$$\mathcal{H}_{\text{ex}} = -2\sum_{i\neq j}^{N} J_{ij}\vec{S}_i \cdot \vec{S}_j \tag{2.1}$$

The interaction is effective between two molecular orbitals i and j with the corresponding spins $\vec{S}_i$ and $\vec{S}_j$. It results from the Coulomb interaction and the Pauli principle [Kit06] [Aha00], where it is described that the complete wave function of two overlapping wave functions need to be antisymmetric in case of fermions.

J_{ij} in Eq. 2.1 is the exchange integral, with J_{ij}=J_{ji} and is given as follows [Stö06]

$$J_{ij} = \int\int \Psi_i(\vec{r_1})\Psi_j(\vec{r_2})\frac{e^2}{4\pi\epsilon_0 r_{12}}\Psi_i^*(\vec{r_2})\Psi_j^*(\vec{r_1})d\vec{r_1}d\vec{r_2} \tag{2.2}$$

It includes the complete wave function which is a product of the spatial $\Phi(\vec{r_1}, \vec{r_2})$ and the spin wave function $\chi(\vec{s_1}, \vec{s_2})$

$$\Psi(\vec{r_1}, \vec{r_2}, \vec{s_1}, \vec{s_2}) = \Phi(\vec{r_1}, \vec{r_2}) \cdot \chi(\vec{s_1}, \vec{s_2}) \tag{2.3}$$

The exchange integral depends on the direct overlap of the molecular orbitals of i and j and takes into account the complete wave functions for both atoms i and j. In a ferromagnetic system the energetically favorable positioning of the spins is a parallel spin orientation, $J_{ij} > 0$. If $J_{ij} < 0$, an antiparallel ordering is energetically preferred.In macroscopic ferromagnetic systems, ferromagnetic exchange leads to spontaneous magnetization and the formation of magnetic domains with a saturation magnetization M_S. The exchange length in a magnetic system is defined as [Abo13]:

$$l_\mathrm{ex} = \sqrt{\frac{2A}{(\mu_0 {M_S}^2)}} \tag{2.4}$$

with the saturation magnetization M_S and the exchange constant $A = x \cdot J_\mathrm{ex} S^2/a$ with $x = 1$ for a simple cubic lattice, $x = 2$ for a body centered cubic lattice and $x = 4$ for a face centered cubic lattice. a is the lattice constant. For the studied sample system in this work, magnetite, which does not belong to the class of $3d$ metals with itinerant magnetism, other exchange interactions have to be considered. The exchange interaction can only describe the direct overlap of of the electron wave functions, yet, in magnetite there are indirect exchange interactions. Those interactions are super-exchange interaction and double-exchange interaction. Super-exchange interaction is defined as the indirect interaction between mainly 3d lattice atoms with the magnetic moments over interstitial diamagnetic atomic 2p orbitals [And50]. Figure 1 shows the mechanisms of direct (a), super- (b) and double- (c) exchange interactions. The super-exchange interaction (Fig. 1(b)) is depicted as the indirect exchange in Fe_3O_4 over an O^{2-} ion with a closed p-shell. Neighboring iron ions overlap with the interstitial electron shell of the

oxygen ion. The coupling mechanism then leads to an antiferromagnetic coupling between the Fe^{3+} ions. The double-exchange mechanism is, contrary to the super-exchange interaction, ferromagnetic. Figure 1 (b) depicts the mechanism for double-exchange. It can be understood as the hopping of an electron from one Fe ion over the diamagnetic 2p O^{2-} orbitals. As the p shells are filled the transfer of the spin proceeds in two steps leading to a ferromagnetic coupling [Zen51].

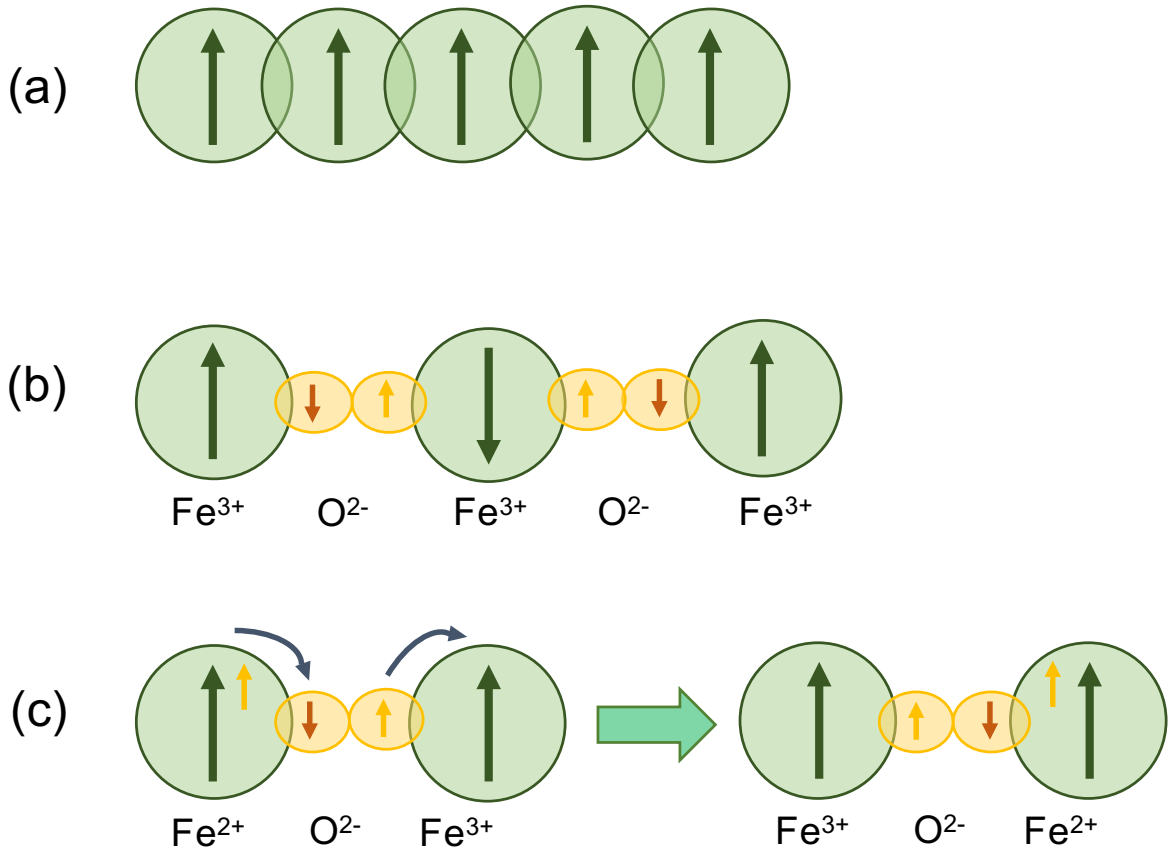

Figure 1: (a) direct exchange (b) super-exchange interaction (c) double-exchange interaction.

2.2. Magnetocrystalline Anisotropy

As the crystallographic structure strongly influences the direction of magnetization, spin orbit coupling affects the magnetic behavior of a material and is one source of the magnetocrystalline anisotropy (MCA). Its energy is dependent on the magnetization axis inside the given crystalline structure. In a system with uniaxial anisotropy the magnetocrystalline anisotropy F_{uni} is defined as follows

$$F_{\text{uni}} = K_0 + K_2 \sin^2\theta + K_4 \sin^4\theta + ... \tag{2.5}$$

with θ as the angle between the magnetic easy axis and the magnetization and material specific parameters K_i. In a cubic system the magnetocrystalline anisotropy can be described as the difference of the energy between the direction cosine along the three cubic edges, called α_i. The direction cosine is the normalized projection of the given magnetization direction $\vec{M}$ onto the crystallographic axes in the system, $\alpha_i = \frac{\vec{M}}{|M|}\vec{e_i}$. The anisotropy for a cubic system (Fe, Ni) with material specific parameters K_4 (as the first non vanishing order of anisotropy constants) and K_6 (the second order anisotropy constant) is given as [Chi97]:

$$F_{\text{cub}} = K_0 + K_4(\alpha_1^2\alpha_2^2 + \alpha_2^2\alpha_3^2 + \alpha_3^2\alpha_1^2) + K_6(\alpha_1^2\alpha_2^2\alpha_3^2) + ... \tag{2.6}$$

Figure 2 shows a polar plot of the surface of the free energy density F_{cub} in a cubic symmetry for both $K_4 > 0$ (2 (a)) and $K_4 < 0$ (2 (b)). The arrows indicate the different crystallographic orientations. In polar coordinates with

$$\alpha_1 = \cos\varphi \sin\theta; \alpha_2 = \sin\varphi \sin\theta; \alpha_3 = \cos\varphi \tag{2.7}$$

and θ as the angle between the magnetization and [001] and φ the angle in the (001) plane, the magnetocrystalline anisotropy in a cubic system can be given as follows

$$F_{\text{cub}}(\theta,\varphi) = \frac{K_4}{4}(\sin^4\theta \sin^2 2\varphi + \sin^2 2\theta) + \frac{K_6}{16}\sin^2\theta \sin^3 2\theta \sin^2 2\varphi + ... \tag{2.8}$$

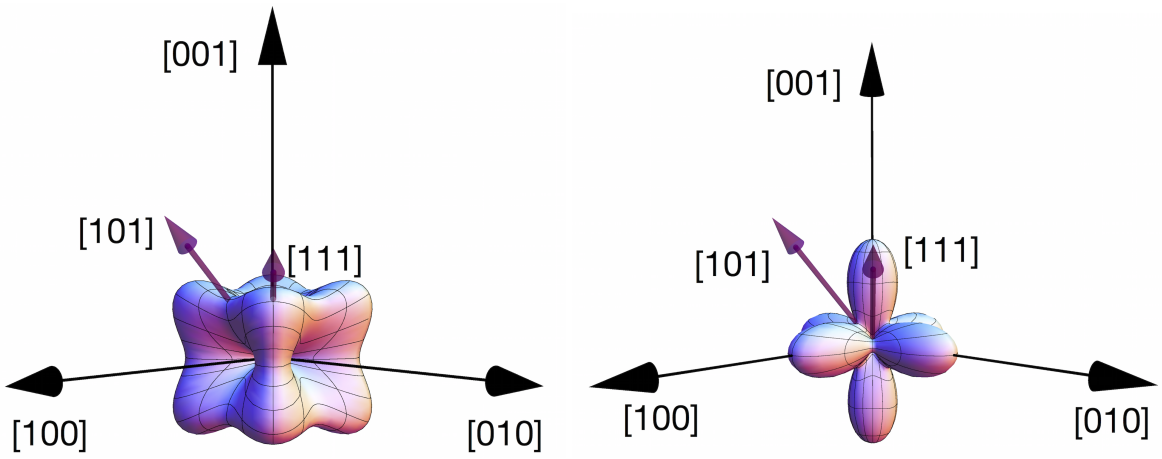

(a) $K_4 > 0$ (b) $K_4 < 0$

Figure 2: Cubic anisotropy energies depicted for a cubic crystal (a) with the magnetic easy axis along the double zero directions and the hard axis along [111] ($K_4 > 0$) and for cubic crystal (b), with the magnetic easy axis along [111] and the hard direction along double zero ($K_4 < 0$).

2.3. The g-factor

The magnetic moment of an atom is only dependent on the angular momentum $\vec{L}$. It can be written as

$$\vec{\mu_L} = -g\mu_B \frac{\vec{L}}{\hbar} \tag{2.9}$$

with the Landé g-factor, and the Bohr magneton $\mu_B = \frac{e\hbar}{2m_e}$ [Kit06]. The orbital Landé g-factor g_l is equal to 1. Due to spin orbit coupling g_j is a combination of $g_l + g_s$. The total magnetic moment results in

$$\vec{\mu_J} = -g_j\mu_B \frac{\vec{J}}{\hbar} \tag{2.10}$$

The g-factor now is

$$g_j = 1 + \frac{J(J+1) + S(S+1) - L(L+1)}{2J(J+1)} \tag{2.11}$$

and the effective net magnetic moment can be then given as $\mu = g_j\mu_B\sqrt{J(J+1)}$ [Gro14]. In crystals which exhibit a cubic crystallography, the orbital moment is quenched, which

reduces its value [Boz03]. The g-factor therefore cannot be described by the Landé g-factor g and needs to be corrected. The value of this new effective value of g, which usually is greater than 2 [Kit49]. Its corrected form can be written as [Mey61]:

$$g = 2 + \left(1 + \frac{\mu_l}{\mu_s}\right) \tag{2.12}$$

2.4. Shape Anisotropy

The demagnetizing effect of the boundaries of a single domain state ferromagnetic material acts back on the direction of the magnetization. This phenomenon is called shape anisotropy and is caused by long range dipolar coupling of the magnetic moments. This coupling decays with $\frac{1}{r^3}$, with r as the spacing between single magnetic moments [Gro14]. [Stö06].

Considering Maxwell's equation $\nabla \cdot \vec{B} = \nabla \cdot \left(\mu_0 \left(\vec{H} + \vec{M}\right)\right) = 0$, the dipolar field (stray field) is due the magnetization divergence $\nabla \cdot \vec{H}_\mathrm{d} = -\nabla \cdot \vec{M}$, as a magnetic monopole can not exist. The internal magnetic field $\vec{B}_\mathrm{int}$ that builds up inside a magnetic material has the following form:

$$\vec{B}_\mathrm{int} = \vec{B}_\mathrm{ext} - \mu_0 \cdot \underline{\underline{N}} \cdot \vec{M} \tag{2.13}$$

$\mu_0 = 4\pi \cdot 10^{-7} \frac{\mathrm{Vs}}{\mathrm{Am}}$ is the magnetic permeability and $\underline{\underline{N}}$ is the demagnetization tensor. For simple geometries this tensor can be calculated. The overall demagnetization field H_d can then be defined as follows:

$$\vec{H}_\mathrm{d} = -\underline{\underline{N}} \cdot \vec{M} \tag{2.14}$$

The energy of this demagnetization field is given as the integral over the volume of the field and the overall magnetization of the magnetic volume.

$$E_\mathrm{d} = -\frac{1}{2}\mu_0 \int \vec{H}_\mathrm{d} \cdot \vec{M} dV \tag{2.15}$$

With this given energy E_d the contribution to the free energy functional can be written as:

$$F_{\text{shape}} = \frac{E_{\text{d}}}{V} \tag{2.16}$$

2.5. Electron Paramagnetic Resonance

In a homogeneous external magnetic field, a paramagnetic system experiences a split of its energy levels with an energetic difference of $\Delta E = g\mu_B B_{\text{ext}}$ as depicted in Figure 3. By applying a microwave photon with the same energy ΔE, a single spin is lifted from the parallel ground state into the higher, exited state. This happens in a paramagnetic material independently from other surrounding spins.

Providing energy with an electromagnetic wave, in this case a microwave, whose ω corresponds to the same energy range as the degeneracy energy produced by the external field $\Delta E = \hbar\omega$ to the system, the system experiences resonance, if the wave is perpendicular to the applied external B-field [Von66] (see Fig. 3).

$$\Delta E = g\mu_B B_{ext} = \hbar\omega \tag{2.17}$$

Resonance requirements are: $\omega = \omega_L$ and a microwave with the frequency $f = \frac{\omega}{2\pi}$.

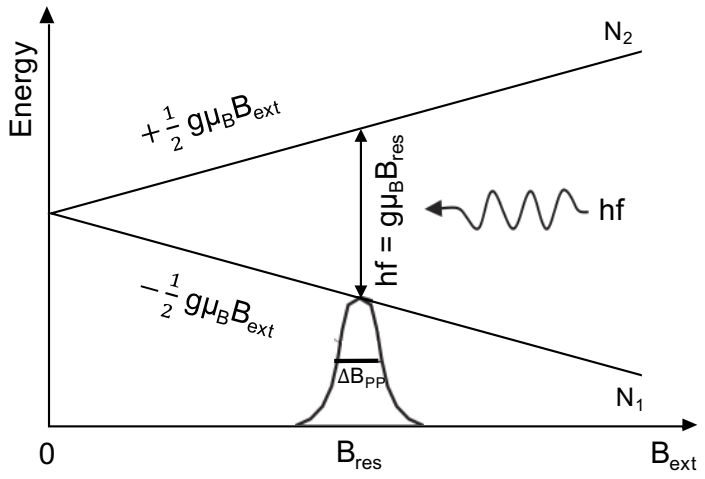

Figure 3: Shown are the Zeeman energy levels N_1 and N_2 in an external magnetic field B_{ext}, with corresponding resonance condition and line width B_{pp} at a resonance position B_{res}.

If this condition is satisfied, there is an absorption of the microwave energy. The resonance field B_{res} can be described as follows.

$$\omega = \frac{g\mu_B}{\hbar} B_{\mathrm{res}} = \gamma B_{\mathrm{res}} \tag{2.18}$$

In a homogeneous external magnetic field $\vec{B_{\mathrm{ext}}}$, a magnetic dipole $\vec{\mu}$ is affected by an angular momentum and experiences a torque. Considering classical laws of motion, the angular momentum $\vec{D}$ will move according the following equation

$$\vec{D} = \vec{\mu} \times \vec{B_{\mathrm{ext}}} \tag{2.19}$$

The magnetic moment without exchange interaction (paramagnet) will precess around the applied external magnetic field. Taking into account the sum of all magnetic moments, the motion of the magnetization $\vec{M}$ in an external field is given by the equation as follows:

$$\frac{d\vec{M}}{dt} = -\gamma[\vec{M} \times \vec{B_{\mathrm{ext}}}] \tag{2.20}$$

with the gyromagnetic ratio $\gamma = \frac{g\mu_{\mathrm{B}}}{\hbar}$. g is the previously discussed Landé g-factor and the Bohr magneton μ_{B}. This will lead to a Larmor precession at $\omega = \omega_L = \gamma B_{\mathrm{ext}}$ [Stö06].

2.6. Ferromagnetic Resonance

In a system with coupled magnetic moments, a ferromagnet, exchange interaction (see chapter 2.1) has to be taken into account. The excitation of this system is contrary to electron paramagnetic resonance (EPR) a collective excitation of the coupled magnetic moments. Those collective excitations are called spin waves, or in a quantum mechanical term, magnons.

Like in a paramagnetic system, the magnetic moments precess around the applied effective field but are treated as a uniform magnetization $\vec{M}$, a macrospin. The time evolution of the magnetization of a ferromagnetic system in an effective magnetic field B_{eff} can be described by the Landau-Lifshitz equation. B_{eff} consists of the internal mag-

netic field due to magnetic anisotropies and the applied external field B_{ext}. The Landau Lifshitz equation is as follows:

$$\frac{d\vec{M}}{dt} = -\gamma[\vec{M} \times \vec{B_{\text{eff}}}] \tag{2.21}$$

This equation is valid for systems without damping. In reality an exited state has a certain lifetime, which is shown in the experiment as damping of the resonant mode, which forces the magnetization into its equilibrium position. This damping affects the magnetization to spiral inwards as a torque motion on a sphere, see Fig. 4 (a).
The damping of the magnetization results from two sources. First there is the lattice coupling and second the interaction between magnons, which will be discussed in the following chapter 2.8. Due to lattice coupling, energy is transferred to the crystal lattice, which results in an overall damping of the resonant mode. Due to the energy losses from damping, the Landau Lifshitz equation has to contain an additional term that accounts for damping effects. The resulting Landau-Lifshitz-Gilbert equation [Gil04] includes the magnetization dynamics and the damping due to spin orbit coupling in the Gilbert damping term with α as the Gilbert damping factor given from the relaxation time:

$$\frac{d\vec{M}}{dt} = -\gamma[M \times B_{\text{eff}}] + \frac{\alpha}{M}[\vec{M} \times \frac{d\vec{M}}{dt}] \tag{2.22}$$

For small sample dimensions as in nanoparticles only a uniform excitation mode inside the particles can be assumed and magnon magnon interaction can most likely be neglected. However, as nanoparticle assemblies can exhibit dipolar interactions, more details will be given in chapter 2.8.

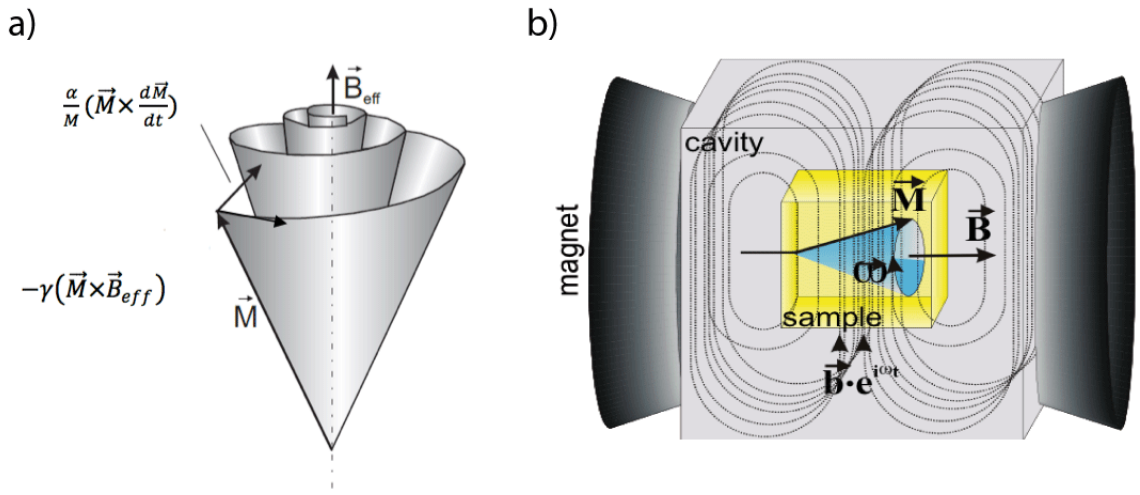

Figure 4: (a) Model of spin precession in a damped system with applied external magnetic field. (b) Standing waves inside a hollow cavity in an external magnetic field as used in conventional FMR measurements, shown is the precession of the magnetization around the external magnetic field and the high frequency B-field of the microwave $\vec{b}\cdot e^{i\omega t}$ perpendicular to $\vec{B_{\text{ext}}}$. Picture taken from [Mec08].

Figure 4 (b) shows the excitation and precession of a collective magnetization inside a ferromagnet around an external magnetic B-field. By keeping a static microwave excitation, the magnetic moment precesses around the external magnetic field in resonance, thus making it possible to detect a resonant absorption in field sweep mode of the set up.

2.6.1. Measurement Signal and Magnetic Susceptibility

For a further understanding on how magnetic properties can be measured with ferromagnetic resonance, the free energy density of the magnetization has to be considered. The magnetization $\vec{M}$ is connected to the free energy of the magnetization F_{M} via the following equations:

$$\vec{M} = \vec{M}_s + \vec{m} \cdot e^{i\omega t} \tag{2.23}$$

The effective magnetic B-field B_{eff} consists not only of the magnetic field component $b_1 \cdot e^{i\omega t} \cdot \vec{e_x}$ in the x-direction produced by the microwaves and the z component of the applied external field, $B_{\text{ext}} \cdot \vec{e_z}$ but also of the internal field inside the sample produced by the magnetic anisotropy of the sample system.

$$\vec{B_{\text{eff}}} = \begin{pmatrix} b_1 \cdot e^{i\omega t} \\ 0 \\ B_{\text{ext}} \end{pmatrix} + \begin{pmatrix} F_{M_x} \\ F_{M_y} \\ F_{M_z} \end{pmatrix} \tag{2.24}$$

$$F_{M_i} = \frac{dF_A}{dM_i} \tag{2.25}$$

All the relevant anisotropy contributions are included in the free energy density $F_{\text{A}} = F_{\text{crystal}} + F_{\text{shape}} + F_{\text{surface}}$. Therefore it is possible to gain information on the anisotropy parameters of a system by measuring the high frequency susceptibility tensor χ''_{xx} [Mec97]. To obtain our measurement signal equation 2.23 has to be solved in the following form

$$\vec{m} = \underline{\underline{\chi}} \vec{b} \tag{2.26}$$

The high frequency susceptibility tensor hereby has the following form

$$\underline{\underline{\chi}} = \begin{pmatrix} \chi_{xx} & \chi_{xy} & 0 \\ \chi_{yx} & \chi_{yy} & 0 \\ 0 & 0 & 0 \end{pmatrix} \tag{2.27}$$

With an external magnetic field in the sample plane, only the following component of the high frequency susceptibility tensor χ_{xx} has to be considered. It is a complex value and consists of a real and imaginary part

$$\chi_{xx} = \chi'_{xx} - i\chi''_{xx} \tag{2.28}$$

In a conventional microwave resonator (cavity) with a standing wave mode, the absorbed microwave signal is directly proportional to imaginary part of χ_{xx}, which is the dissipative part of the microwave. χ'_{xx} is hereby the frequency dependent dispersive part.

The absorption signal results in a Lorentzian function for linearly polarized microwaves. Inhomogeneous microwave excitation or slight deviations of the angle of the probing microwave influence the resulting shape of the measured signal and will be discussed in chapter 5.2.

2.7. Free Energy Density

As described in chapter 2.6.1 the measured signal in FMR is partly made of the free energy density of the probed material. The overall magnetic anisotropy contributions can be described by the free energy density functional F. In order to turn the magnetization from its energetically preferred direction to a non preferred one, this energy must be overcome. The free energy density functional depends strongly on the crystalline orientation in the material, its shape, interfaces and surfaces. They affect the magnetization in a material, resulting in non equal magnetization orientations.

$$F = F_{\text{zeeman}} + F_{\text{A}} = F_{\text{zeeman}} + F_{\text{crystal}} + F_{\text{shape}} + F_{\text{surface}} \tag{2.29}$$

The overall free energy density term is made up by four anisotropy contributions. It consists of the Zeeman energy $F_{\text{Zeeman}} = -\vec{M} \cdot \vec{B}_{\text{ext}}$ (energy levels in external magnetic field ($B_{\text{ext}} \neq 0$)), which is the only isotropic part, the magnetocrystalline anisotropy F_{crystal} as described in chapter 2.2, the shape anisotropy F_{shape}, see chapter 2.4, and the surface anisotropy F_{surface} which is a contribution resulting from a symmetry break of the crystallographic structure at the surfaces. The non continuity of the periodical crystal structure at the surface affects the magnetic moments on this location. The inner magnetic moments experience a different anisotropy field compared to the magnetic moments located at the surface or interfaces, due to stray field formation. These effects give rise to the overall anisotropy [Kit06] [Stö06].

2.8. Collective Magnetic Excitations

Collective magnetic excitations, or spin waves, can be described as an oscillation in the relative orientation of magnetic moments in a lattice. The net moment of the magnetization stays constant, resulting in only 2 degrees of freedom for the coherent precession. Their description follows Bose-Einstein statistics as they are quasiparticles with a full numbered spin. The exchange coupled spins will have a phase shift and a wave vector $\vec{k}$. Figure 5 shows a model of the coupled spin precession. For small wavelength of the spin waves, the exchange interaction as described in chapter 2.1 dominates, and the resulting modes are called exchange modes [Gro14].

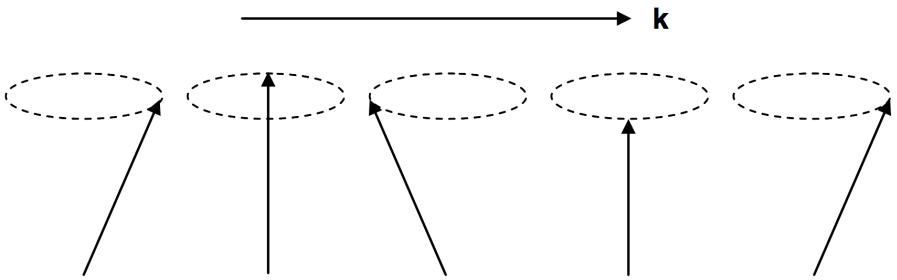

Figure 5: Visualization of a spin wave as a disturbance in which the angle of precession varies linearly from spin-to-spin in the direction of propagation, picture from [Sta08].

The exchange energy inside a spin wave can be described by the following equation:

$$E_{\text{ex}} = -\frac{J_{\text{ex}}}{\hbar^2} \sum_{i=1}^{N} \vec{S}_i \cdot (\vec{S}_{i-1} + \vec{S}_{i+1}) \tag{2.30}$$

The dispersion relation for spin wave is given as follows

$$\omega = \gamma B + \frac{2J_{\text{ex}}S}{\hbar^2}(1 - \cos(ka)) \tag{2.31}$$

As described in chapter 2.6, ferromagnetic resonance is a collective magnetic excitation. The studied nanoparticle system is strongly coupled due to dipolar interactions between the particles. Therefore the observed magnetic system does not only experience uniform

excitation modes but also magnetostatic modes. In case of long wavelengths for the wavevector $\vec{k}$, the influence of magnetic anisotropies rises and becomes dominant over the exchange between two spins. As long as the microwave excitation still is in a linear regime a splitting of the collective excitation modes can not be observed. Due to damping the excitations with a uniform excitation mode decay and the length of the magnetization will be no longer constant [Lin02]. Assuming uniform excitation in the linear microwave regime, the magnons are coupled due to dipolar interactions, resulting in dipolar coupled modes, which can be distinguished by their relative orientation to the external magnetic field. Those resulting modes are as follows [Gro14] [vG93]

- Damon-Eshbach Mode - the wave vector $\vec{k}$ is parallel to the sample surface and perpendicular to $\vec{B_{\text{ext}}}$, the precession amplitude decays exponentially into the sample
- Forward Volume Mode - the wave vector $\vec{k}$ is parallel to the sample surface and perpendicular to the applied external magnetic field $\vec{B_{\text{ext}}}$ which is perpendicular to the sample surface, the precession amplitude is not only located at the sample surface but oscillates inside the sample
- Backward Volume Mode - imaginary wave vector $\vec{k_{\text{x}}^{i}}$, exhibits a negative group velocity opposite to the phase velocity, the wave vector is parallel to the sample surface and parallel to the applied external magnetic field $\vec{B_{\text{ext}}}$ which is also parallel to the sample surface
- Magnetostatic Surface Mode - imaginary wave vector $\vec{k_{\text{x}}^{i}}$

2.9. Magnetite - Fe_3O_4

In this work the magnetic properties of magnetite nanoparticles has been studied. Magnetite, $FeO{\cdot}Fe_2O_3$, belongs to the class of spinel ferrites, which are generally described as $MO{\cdot}Fe_2O_3$, where M is the representation of divalent metal ions. It has an inverse spinel fcc structure with a unit cell consisting of 8 formular units of Fe_3O_4 (56 ions), belonging to the $Fd3m$ space group (cell size a=8.39 Å [Fai08b]). One unit cell of a spinel consists of eight fcc oxygen cells (32 O^{2-} ions). The A-sites are occupied by 8 Fe^{3+} ions, each surrounded by a tetrahedral oxygen coordination and the B-sites are surrounded by an octahedral coordination of oxygen, with the B-sites occupied with equal Fe^{2+} and Fe^{3+} ions (16 in total). [Chi97]. Figure 6 shows the crystal structure of magnetite with the A-sites occupied by Fe^{3+} ions and the B-site occupied with Fe^{2+} and Fe^{3+} ions.

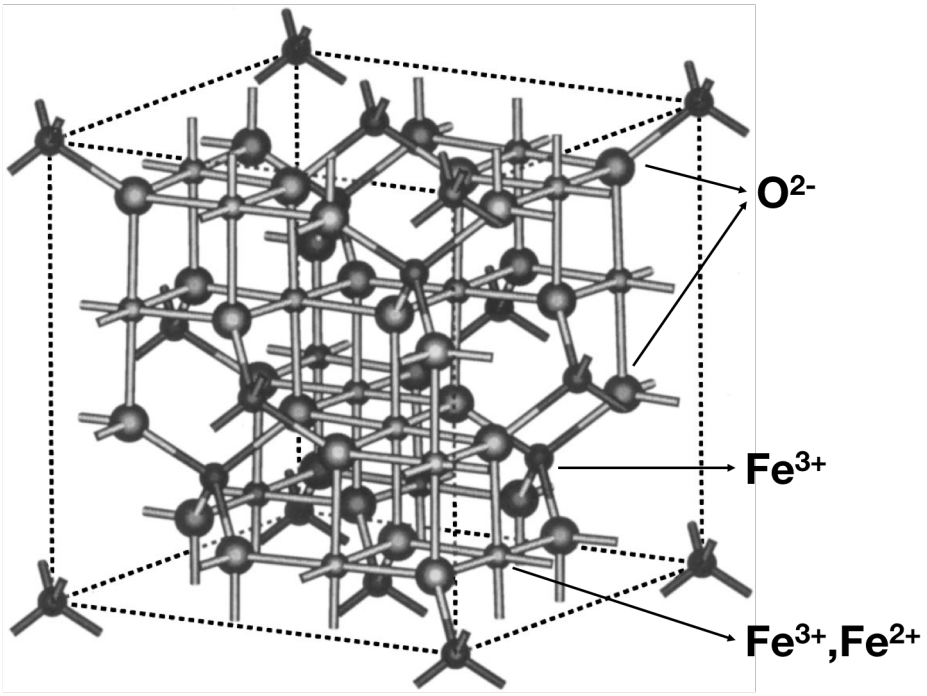

Figure 6: Crystal structure of Fe_3O_4, inverse spinel fcc with oxygen and iron atoms as depicted, the close packed fcc consists of oxygen with iron at the interstitial sites. Picture from [Jen02].

In magnetite the spins of Fe^{3+} in the tetrahedral and octahedral coordinations are antiferromagnetically coupled through super-exchange (as explained in chapter 2.1), the Fe^{2+} and Fe^{3+} ions in octahedral coordination are ferromagnetically coupled through double-exchange. Due to the super- and double-exchange, only the Fe^{2+} and Fe^{3+} ions in octahedral coordination contribute to the overall saturation magnetization. Magnetite therefore is a ferrimagnetic material below a temperature of $T_C = 860\,\mathrm{K}$. [Gro14] Magnetite undergoes a first order phase transition, namely Verwey tansition, at $T_\mathrm{V} = 120\,\mathrm{K}$ from metallic to insulating behavior [Stö06]. At this temperature it exhibits a crystallographic transition. The saturation magnetization of magnetite above T_V is given as $M_{sat} = 4.6 \cdot 10^5\,\frac{\mathrm{A}}{\mathrm{m}}$ [Bic50]. The body diagonal, the [111] direction is its easy axis of magnetization. The magnetic anisotropy constant K_4 (see eq. 2.6) has been experimentally determined via FMR measurements by Bickford [Bic50] and from magnetization measurements along different crystallographic axes by Kakol and Honig [Kąś9]. The following table shows an overview of the different anisotropy constants. The value of K_4 of magnetite crystals is in the range of $-1.26 \cdot 10^4\,\frac{\mathrm{J}}{\mathrm{m}^3}$ to $-1.14 \cdot 10^4\,\frac{\mathrm{J}}{\mathrm{m}^3}$.

Values of K_4, K_6 and g_eff at room temperature		
	Bickford	Kąkol/Honig
$K_4[\frac{\mathrm{J}}{\mathrm{m}^3}]$	$-1.1 \pm 0.08 \cdot 10^4$	$-1.2 \pm 0.06 \cdot 10^4$
$K_6[\frac{\mathrm{J}}{\mathrm{m}^3}]$		$-0.3 \pm 0.06 \cdot 10^4$
g_eff	2.12 ± 0.04	

Table 1: Experimentally extracted values for the first, K_4, and second K_6 non vanishing order of the magnetocrystaline anisotropy as well as g_eff after [Bic50] and [Kąś9] for magnetite single crystals. Measurements have been performed at 295 K.

3. Magnetospirillum Gryphiswaldense

Magnetotactic bacteria (MTB) first have been described as magnetoresponsive microorganisms by Bellini [Bel63] and Blakemore [Bla75]. Those bacteria are able to navigate in magnetic fields and are found in aquaeous marine, as well as in fresh water surroundings [Sch08]. The magnetic navigational sense of the bacteria is called magnetotaxis. They use this sense to navigate inside the geomagnetic field. The magnetism in the bacteria arises from biomineralized nanoparticle chains which are encapsulated inside the cell body. These nanoparticles are located inside an organelle, called magnetosome. A magnetosome consists of a lipid bilayer membrane with a thickness of approximately 5 nm [Fai15]. The magnetosomes with the particles inside are attached to a cytoskeletal filament structure, which serves as an anchor to the magnetosomes, aligning the nanoparticles. Along the filament, the magnetic nanoparticles are typically oriented along their easy axis of magnetization, resulting in a dipole like behavior for a single bacterium. The nanoparticles inside the bacteria can either consist of magnetite (Fe_3O_4) or greigite (Fe_3S_4) [Fai08b]. Several different strains of magnetotactic bacteria are known today. Each strain exhibits a strain specific particle size, morphology and chain length, as well as number of chains (for example *Magnetobacterium Bavaricum* with up to 1000 particles per cell, see Figure 7 [Han96] (c)). Additionally also the shape of the bacterias cell body and/or number of flagellae can differ. Cell body, particle size, chain number and length, however, remain constant for a specific strain as they are genetically controlled. The particle morphologies in magnetotactic bacteria vary from bullet shaped particles, cuboctahedral particles to elongated cuboctahedral particles as visualized in Figure 7 [Sch08] [Fai08b] [Fai15].

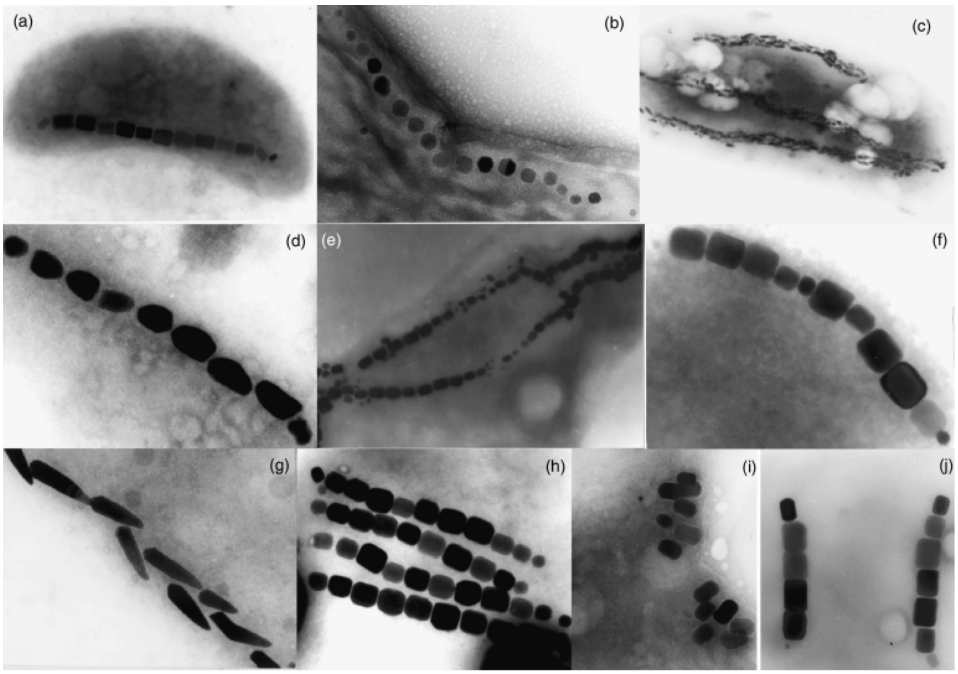

Figure 7: Transmission electron pictures of the various possibilities of different magnetosome morphologies. Crystals in magnetotactic bacteria might exhibit an elongated prismatic shape (a, e, f, h, i, j), cuboctahedral (b) or bullet-shaped morphologies (c, d, g). The different occurring morphologies can be in single or multiple chains. Picture from [Sch08].

The bacteria used throughout this work are all magnetotactic bacteria of the strain *Magnetospirillum Gryphiswaldense* (MSR-1) in their wild type configuration and mutations thereof. This strain has helicoidal/spirillum cellbodies and produce cuboctahedral magnetite particles in a size range of $30 - 50\,\mathrm{nm}$. The nanoparticle chains generally consist of typically $20 - 30$ magnetosomes [Fai15]. Brightfield transmission electron microscopy was used to picture the different bacteria cultured and used in this work. Figure 8 a) shows a bacterium of the wild type. It is filled with a chain of 17 nanoparticles, without any distortions inside the chain, but slight differences in the particle size. Figure 8 b) depicts a mutation ($\Delta Mamk$) of the wild type. It can be seen that the particle chain exhibits distortions, the chains are double or broken as this mutation lacks

of the anchoring protein to the cytoskeletal filament. The mutations will be discussed in chapter 3.2.

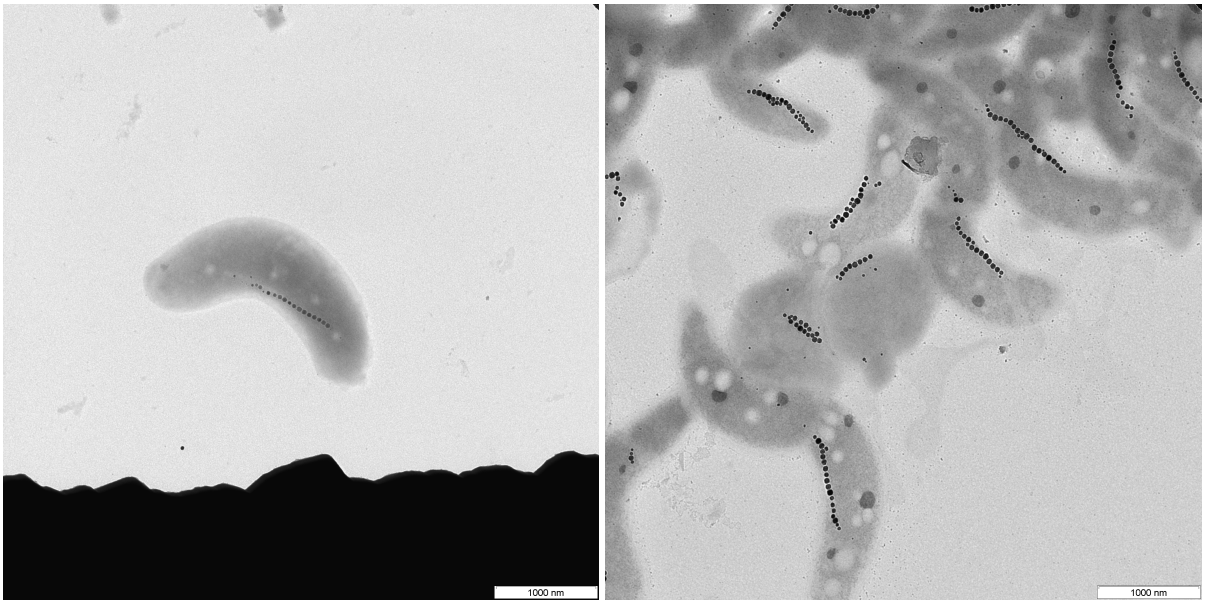

(a) Wild Type (b) $\Delta Mamk$

Figure 8: (a) Transmission Electron Microscope image of MSR-1 wild type bacterium, showing a single chain and of (b) MSR-1 $\Delta Mamk$ bacteria, showing broken chains because the magnetosomes are not aligned along the cytoskeletal filament properly, picture courtesy of S. Ghaisari, Max Planck Institute for Colloids and Surfaces, Potsdam-Golm

3.1. Biomineralization

Biomineralization is a term used for either a biologically induced or a biologically controlled process. Biologically induced mineralization takes place extracellular and is not a genetically controlled process, whereas biologically controlled mineralization happens extra-, inter- or intracellulary. The formation of biominerals in terms if nucleation, growth rate and morphology are genetically set [Fai15], leading to different kinds of particles and chains when genetically modified. Here a wild type of the *Magnetospirillum Gryphiswaldense* and a mutant strain ($\Delta Mamk$) has been experimentally studied.

Biomineralization follows classical nucleation rules. The organism needs to take up the element or combinations thereof. After reaching a supersaturated state, a critical nucleus is formed and with a mineral concentration high enough, ordered crystal growth will start. Chemically, the bacterium forms magnetite ($Fe^{II}Fe^{III}{}_2O_4$) through a complex biochemical process. A model has been proposed Faivre et al [Fai15] [Bau13]. Figure 9 depicts the model of a possible biomineralization pathway. The bacteria take the oxygen out of water, the iron source can be either taken up as Fe^{2+} or Fe^{3+} compounds. The iron crosses the outer cell membrane and intracellularly gets converted into a ferrous high spin species and ferritin. The magnetite forms via a phosphate rich Fe^{3+} hydroxide phase ($Fe^{III}PO_4{}^{3-}$) as depicted in Figure 9. As reaching the inner magnetosome cells, iron and phosphate gets separated. The phosphate gets transported out of the cell and water goes in. Ferrihydrite ($Fe_2O_3{\cdot}nH_2O$) forms.

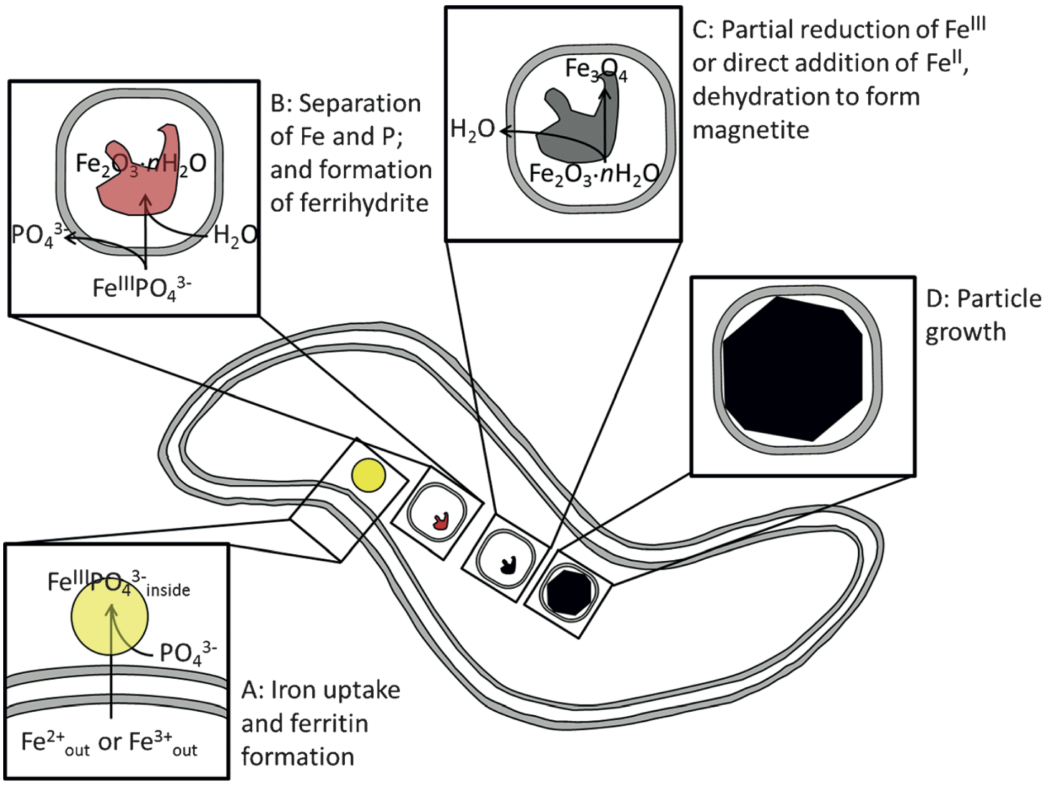

Figure 9: Process of biomineralization inside a bacterium as proposed by Faivre et al., taken from [Fai15].

The ferrihydrite undergoes dehydration or the Fe^{III} gets reduced in order to form magnetite. After reaching a supersaturated phase, a nucleus forms and particle growth starts. Once formed, the magnetite crystal will grow into a nanoparticle. This nanoparticle can have different morphologies, but it is proposed, that magnetite nanoparticles inside the magetotactic bacterium *Magnetospirillum Gryphiswaldense* have a cuboctahedral shape with 8 hexagonally shaped [111] facets and 6 rectangular [100] facets, truncating the perfect octahedral shape of the crystal. In reality, this morphology might be distorted and possible shapes can be assumed for the given crystallographic space group. Figure 10 shows the possible crystallographic shapes, determined by High Resolution Transmission Electron Microscopy (HRTEM) and possible models for resulting crystal shapes.

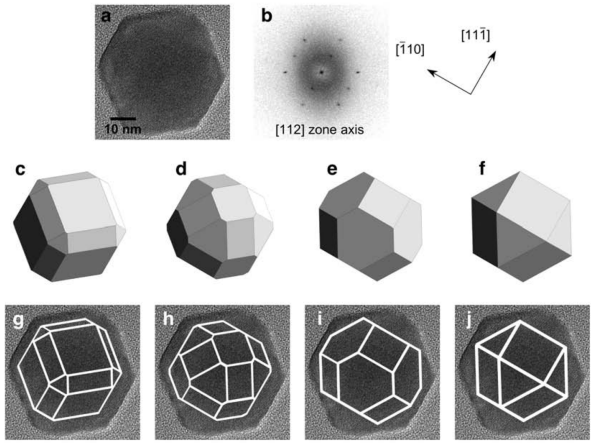

Figure 10: Possible crystalline structures of mature MSR-1 magnetite crystals. (a) HRTEM of a single magnetite crystal (b) Fast Fourier transform (FTT) of image a depicting the crystallographic orientations inside the crystal. (c-f) Models for four different morphologies derived from various combinations of the three crystal forms 111 (octahedron), 100 (cube), and 110 (dodecahedron), shown in the same orientation as the magnetite crystal in a. (g-j) The projected outlines of the models are compared with the magnetosome in a, picture taken from [Fai08a].

3.2. Types and Mutation

As mentioned in chapter 3, magnetotacic bacteria can be genetically modified in order to exhibit different intracellular nanoparticle arrangements. A lipid bilayer encloses the nanoparticles. Its thickness is 5 nm, resulting in a particle interdistance of 10 nm [Fai08b]. The membrane consists of phospholipids and a set of proteins which are responsible for particle growth and arrangements. Mutation of the magnetosome genome results in differently shaped and arranged particles. In this work only *Magnetospirillum Gryphiswaldense* (MSR-1) with the genetic mutations of the proteins responsible for the magnetosome arrangement have been studied. Figure 11 shows the different parts of the bacterium that are affected by the mutations of specific genes.

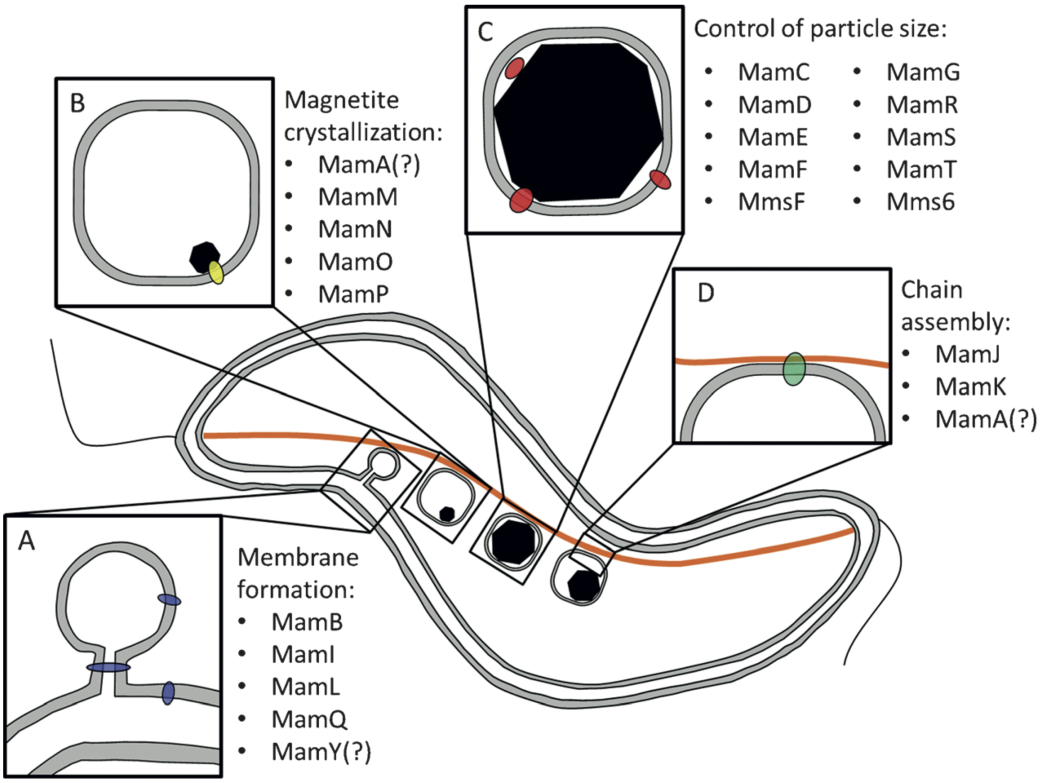

Figure 11: Different proposed sources for different particle size, arrangements and formations inside a bacterium of the type *Magnetospirillum Gryphiswaldense*, taken from [Fai15].

Part A is responsible for the membrane formation. Without these proteins particles can not grow as there is no closed cell in which the particle growth can take place. Mutation of this part can lead to a faulty membrane or no membrane at all. Part B is responsible for the magnetite crystallization. Successful crystal growth is dependent on the existence of those proteins. The particle size is controlled by the proteins depicted in C. A lack thereof might result in bigger or smaller particles. The gene group responsible for the chain assembly are depicted in D. The proteins $MamK$ and $MamJ$ (and possibly $MamA$) are responsible for the chain assembly (Figure 11 D). If the bacterium either lacks $MamK$ or $MamJ$, the particle chain is either broken with interstitial sites or it results in an agglomerate of particles which are not aligned by their easy axis [Sch06]. As described earlier, in this work bacteria of the wildtype and those with a lack of $MamK$ have been magnetically studied. Magnetotactic bacteria can either be extracted from geological samples or cultivated in laboratory environments. The cultivation process of the bacteria can be done either in flasks or in a fermentor [Hey03] [Fai08a]. The bacteria used in this work have been prepared via oxystat cultivation under microaerobic conditions. The bacteria were prepared with feeding solution and iron enriched medium to form the particles, following the procedure described in [Fai08a].

3.3. Bacteria Sample Preparation

Bacteria samples for magnetic measurements were prepared as follows. The bacteria were mixed with HEPES (2-[4-(2-hydroxyethyl)piperazin-1-yl]ethanesulfonic acid) buffer (pH 7) to prevent them from osmotic bursting. The mixture of bacteria, feeding medium and HEPES was then centrifuged at 9000 rpm for 5 min at a temperature of 4 °C. This procedure has been done 4 times. After each centrifuge run the bacteria settled as a pellet at the bottom of the centrifuge flasks and the remaining solution has been removed and substituted after each run with HEPES buffer. The resulting precipitate then was re-disperged in buffer solution. This bacteria solution has been diluted and transferred into a micromanipulator unit. With its help the bacteria could be deposited in a microresonator at the designated sample site (for the setup see the appendix A 39).

4. Magnetic Characterization - FMR

Since their discovery magnetotactic bacteria have been characterized magnetically. Most of those studies concentrate on the magnetic behavior and characterization of bulk material via magnetometry as well as FMR measurements [Abr14] [Fis08] [Geh11b] [Geh11a].

Figure 12 shows a spectrum acquired via FMR in a conventional cavity measurement. The sample here is a bulk sample of MSR-1 wild type bacteria on a silicon oxide substrate. The cultured bacteria cells were aligned by letting a drop of sample solution dry in a homogeneous magnetic field. The drying process inside the magnetic field (permanent magnets, B=500 mT) only led to an alignment of roughly 50 % of the bacteria dropped on the substrate. The experiment has been performed at X-band frequencies and the sample has been measured in-plane, with the external magnetic field along the sample plane and the in-plane alignment, and out-of-plane, with the external magnetic field perpendicular to the sample plane. In the spectrum a distinct difference in between the in-plane and out-of-plane spectra can be seen. In-plane there is a statistical distribution of resonances at a low field at an average position of 238 mT and a width of 44 ± 1 mT. The out-of-plane spectrum shows a statistical distribution of single resonances with average resonance positions of 375 mT and a width of 40 ± 1 mT. Additionally both spectra have a similar broad background signal. Furthermore an EPR (green) signal can be seen in both spectra at the same field position of 314 ± 0.5 mT with a line width of 12 ± 0.5 mT for the in-plane spectrum and 8 ± 0.5 mT for the out-of-plane spectrum. This signal most likely can be ascribed to the buffer solution used in the sample preparation as described before and will be explained in chapter A.5 more closely. The spectrum shows that in-plane it can be assumed to be the easy axis of magnetization along the chains, and the hard axis of magnetization perpendicular to it due to the shift to higher fields as the bacteria are attached to the substrate. In the in-plane component of the spectrum the bacteria are aligned along their nanoparticle chains. Yet, the broadened resonance distribution is due to the dipolar coupled nanoparticles, as the chains are not perfectly aligned and therefore random orientations of the single articles and chains overlap in their resonances which broaden the width of the resulting signal.

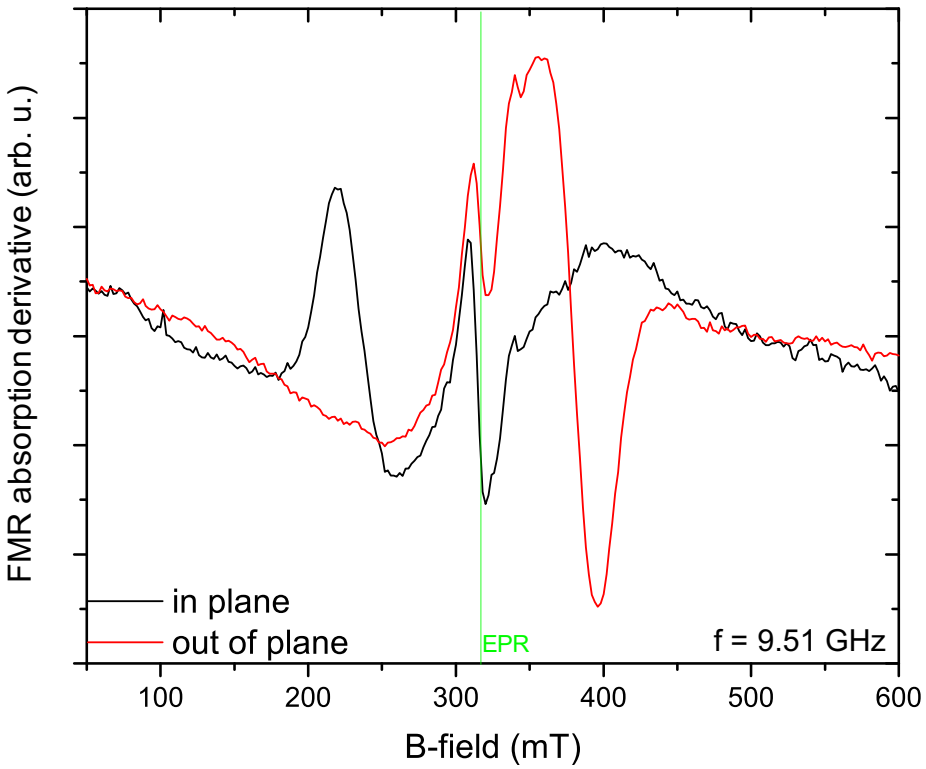

Figure 12: FMR spectrum on an aligned MSR1 wild type bulk sample. Shown is the FMR absorption derivative over the applied external magnetic field, with the black line depicting the spectrum acquired for the in-plane spectrum, and the red line for the out-of-plane spectrum. The green line shows the EPR line of the HEPES buffer. The spectrum was acquired at a frequency of f=$9.51 \pm 1 \cdot 10^{-4}$ GHz with an external field modulation of 2 Gauss.

Figure 13 shows a schematic representation of the coupled nanoparticles inside the magnetosomes. This picture corresponds to the in-plane and out-of-plane spectra on the bulk samples and should simplify the understanding of the coupling of the particles to each other. Is the external magnetic field aligned along the chain axis, acting here as an easy axis of magnetization, the ferromagnetic resonance spectrum will show a

low field peak. Perpendicular to the easy axis of magnetization only the out-of-plane components can be seen, resulting in a high field peak.

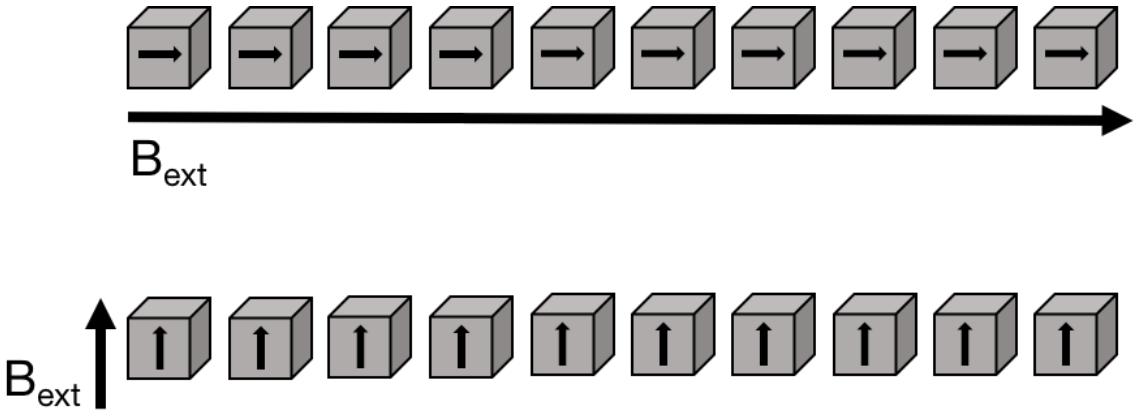

Figure 13: Shematic picture of the particles in an external magnetic field with respect of their magnetization. The upper cain shows the easy axis with an in-plane magnetization along the chains, the lower pictogram shows the corresponding out-of-plane component, the hard axis of magnetization.

In addition to the wild type cells, bacteria with a lack of the MamK protein, called $\Delta MamK$ have been studied. Mutant MSR-1 bacteria have been deposited on a substrate in the same manner as the wild type sample, but without the application of a static magnetic field during the drying of the sample. In Figure 14 the direct comparison of the in-plane and out-of-plane spectra are pictured. Taking into account that the mutation in the $\Delta Mamk$ strain only affects the nanoparticle chains inside the bacteria that there are defects in the chain in terms of their distance, the spectrum acquired should not differ distinctly from the MSR-1 wild type measurement. The measurements have been performed with the same parameters as the wild type measurements . In the in-plane spectrum there is a weakly pronounced and broadened statistical distribution of resonances at a low field peak of 243 mT and a width of 54 ± 0.5 mT, just in the range as the bulk spectra shown in Figure 12 due to the non aligned cells. As the chains are all randomly oriented, all anisotropy contributions overlap and are distributed over the whole measured field range. The out-of-plane spectrum is of a higher intensity with

a statistical resonance field distribution at a field position of 390 mT and a width of 28 ± 0.5 mT but showing a shoulder in the range from $340 - 375$ mT. In the out-of-plane component, the random chain distribution can be neglected, as only the contribution of the magnetic hard axis can be detected (compare Figure 13).

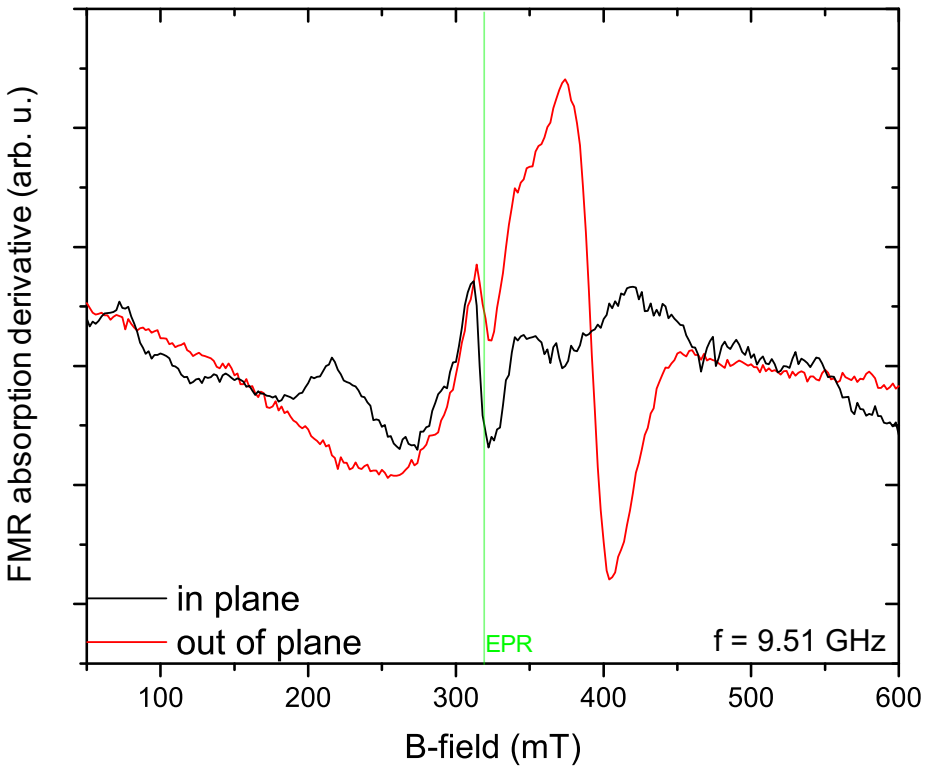

Figure 14: FMR spectrum of unaligned $\Delta Mamk$ bulk sample, the black black depicts the in-plane, red the out-of-plane measurements. Shown is the FMR aborption derivative over the applied external magentic field. Measurement frequency f=$9.51 \pm 1 \cdot 10^{-4}$ GHz, external field modulation of 2 Gauss

Again, the EPR signal of the buffer solution is pronounced in the obtained resonance spectra. Its resonance is at a position of 318 ± 0.5 mT with a line width of 12 ± 0.5 mT for the in-plane spectrum and 10 ± 0.5 mT for the out-of-plane spectrum, lying in in the range of the spectrum of the wild type sample measured before. Hence, this signal can be

attributed to an isotropic EPR centrum and is not an artifact of the measured magnetite nanoparticles. The bulk measurements give a rough estimation about the statistical behavior of the coupled magnetite nanoparticle chains, but lack of information on the single magnetite crystals inside the bacteria cells or a single chain and the interaction between the particles inside the chain. To evaluate the nanoparticles more closely and extract material specific parameters, the system has been downscaled and studied with microresonator FMR.

5. Magnetic Characterization - microFMR

Recently developed microresonator ferromagnetic resonance (microFMR) technique provides the possibility to measure single nanoparticles and different geometrical arrangements of them with a sensitivity of 10^6 [Nar08]. We established a stable system for angular dependent microFMR on single nanoparticles in a sensitivity range corresponding to 20 nm edge length. The microresonators used are operable within X-band frequencies. In this work resonators have been used that were produced via optical lithography and have a resonance frequency of 9 GHz. Because of parallel processed production, the microresonators used throughout this work are of comparable quality ($Q = 108$) and functionality [Mas15].

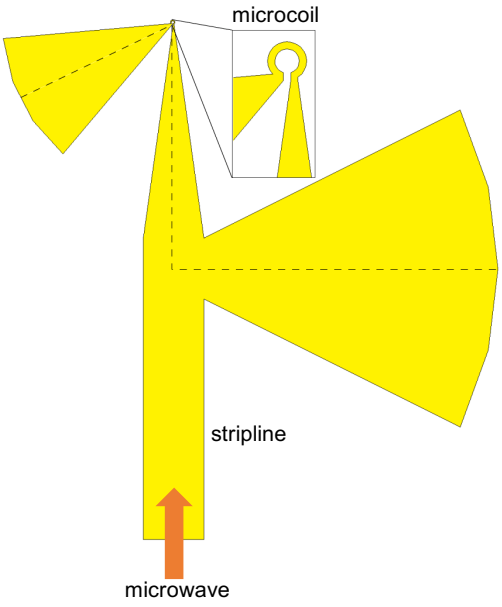

Figure 15: Schematic picture of the microresonator structure used throughout this work, the inset shows a magnification of the resonator loop in which the samples have been placed [Mas15].

5.1. Experimental Setup

A modified sample mounting and waveguiding has been used to incorporate microresonators into a conventional FMR setup, able to handle a full angle dependence [Mas15]. Figure 16 gives a schematic view of the actual measurement setup and the parts used in the experiment. The microwaves used for spectroscopy are generated in a microwave bridge (Type Varian E102). The generated microwaves are in the X-band with frequencies between $8.8-9.6\,\mathrm{GHz}$. The frequencies given throughout this work have an accuracy of $10\,\mathrm{kHz}$, thus all values for the frequencies following are given without an error margin. The microwaves are led through an antenna, mounted at the opening of the klystron, and are guided through a self built semi rigid cable setup with a static phase shift component. The microresonator itself is located between modulation coils, built in the pole shoes of the magnet, and the 180° rotatable electromagnet. The microwave bridge consists of three parts. The first part is the klystron, which generates the microwaves. Part of the microwaves are provided as a reference for a Schottky diode, detecting the reflected microwaves in its quadratic regime, providing an output voltage linearly to the absorbed microwave power in the sample system. The other part of the electromagnetic waves passes a circulator and is led through the semi rigid cable to the sample. The circulator works as a distributor for the electromagnetic waves. This makes it possible to obtain an absorption signal proportional to the magnetic susceptibility, when the sample is in resonance. The Schottky diode is a detector and measures the strength of the microwave absorption. The microwaves are tuned to the resonator's resonance frequency and the maximum of the energy absorbed inside the resonator. For a sensitive detection of the reflected signal, lock-in technique in combination with external field modulation was used. To increase the maximum absorption of the microwave, a static phase shift component for impedance adjustments is used. During the measurement an automatic frequency control (AFC) keeps the setup tuned to the resonance frequency of the microresonator. It maintains the tuning of the frequency during the measurement, regardless of slight frequency changes that occur in resonance during the measurement. Thus it always

provides the maximum possible signal intensity and sensitivity and provides comparable spectra of measurements in a microresonator.

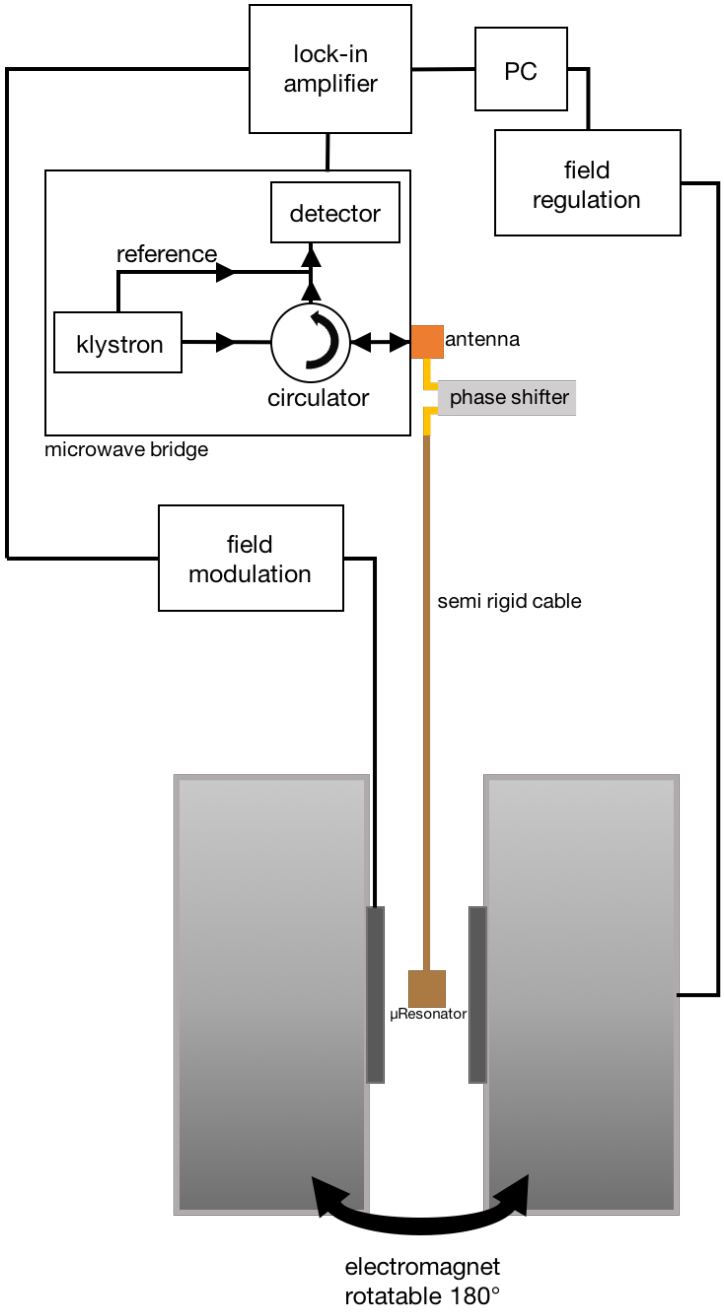

Figure 16: Schematic overview of the experimental setup for microFMR measurements with given parts and components used.

5.2. Line Shape in microFMR

The FMR spectra of the measurements in the microresonators show a distinct deviation from the usually expected line shape. Conventional FMR uses the absorbed component of the B_{hf} field of the linear polarized microwave used for spectroscopy. Hence, as described earlier in chapter 2.6.1, the measurement signal arises from χ'', which is the dissipative part of the microwave. It results in a symmetric line shape as it gives the derivative of a Lorentzian function. By using microresonators for probing samples, the magnetic field B_{hf} is generated by the electrical current through the resonant metallic loop. In contrary to hollow cavity FMR, the current does not arise from B_{hf} of the microwave, but from the oscillating E_{hf} part between the resonant ends of the resonant structure. Thus, during the measurement, the resistance in the resonator changes, and not only the dissipative part of the microwave, but also the frequency dependence dispersive part, χ' is detected. A combination of both the dissipative and dispersive part can generate a characteristic asymmetric line shape. Measurements on a paramagnetic material, DPPH (Di(phenyl)-(2,4,6-trinitrophenyl)iminoazanium), has been used as a model to explain the asymmetric lines. Figure 17 shows an EPR spectrum of a DPPH flake inside a microresonator. It is visible that the EPR absorption derivative over the applied external magnetic field has a very asymmetric behavior. For this given sample the line shape can be attributed to the sample placement close to the resonator loop edge. The distortion of the line shape here is most likely produced by an exciting $\vec{B_{\mathrm{hf}}}$ which is not perpendicular to the external magnetic field.

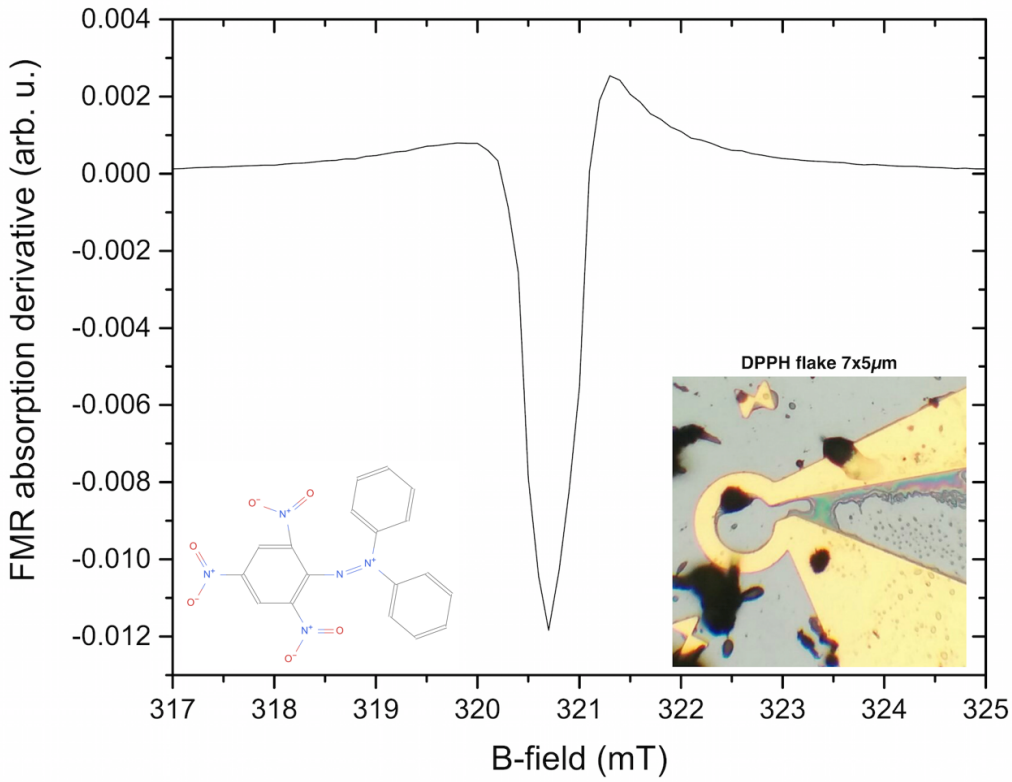

Figure 17: MicroFMR on a $7 \times 5\,\mu$m DPPH flake, $f = 8.987\,$GHz, $f_{mod} = 123.45\,$Hz, *modulation* $= 1.8\,$Gauss, measured with reference and automatic frequency control (AFC), inset on the left depicts the molecular structure of the paramagnetic DPPH, inset on the right shows the deposited DPPH flakes inside the microresonator

Figure 18 schematically shows the magnetic field produced by a current through the loop. Here φ is the angle of the tilt of $\vec{B}_{\mathrm{hf}}$ in the sample plane, θ is the tilt perpendicular to the sample plane.

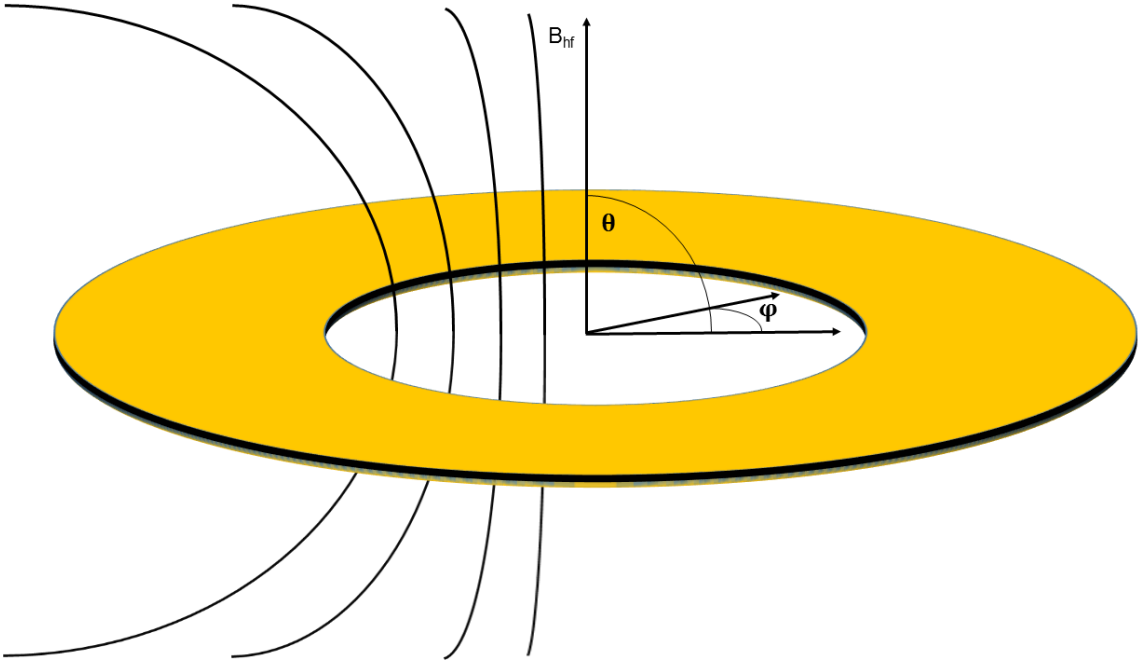

Figure 18: Sketch of the B-field distribution inside a microresonator, here represented as a 2 dimensional disk with loop.

As depicted, the field lines tend to bend closer to the loop structure. Calculations of the expected line shape for the imaginary part of χ generate an asymmetric field line, resulting from a tilted θ angle, see Figure 19. This calculated resonance line shape fits the actual spectrum of DPPH. For further evaluation of resonance line shapes those effects, as well as sample placement has to be taken into account. As we place the sample closer to the edges of the metallic resonant structure, the E-field peaks. This influences the magnetic field lines, leading to distortions and inhomogeneous field distribution. The absence of a completely uniform magnetic field covering the whole sample area is responsible for losses and additional reflections of the microwave, which both influence the resulting line shape of the FMR spectrum. Figure 19 (a) shows a calculated asymmetric spectrum if only χ'' is measured (green). Figure 19 (b) shows the calculation for the same system, but shows the same asymmetry when measuring a combination of χ' and χ'' (blue).

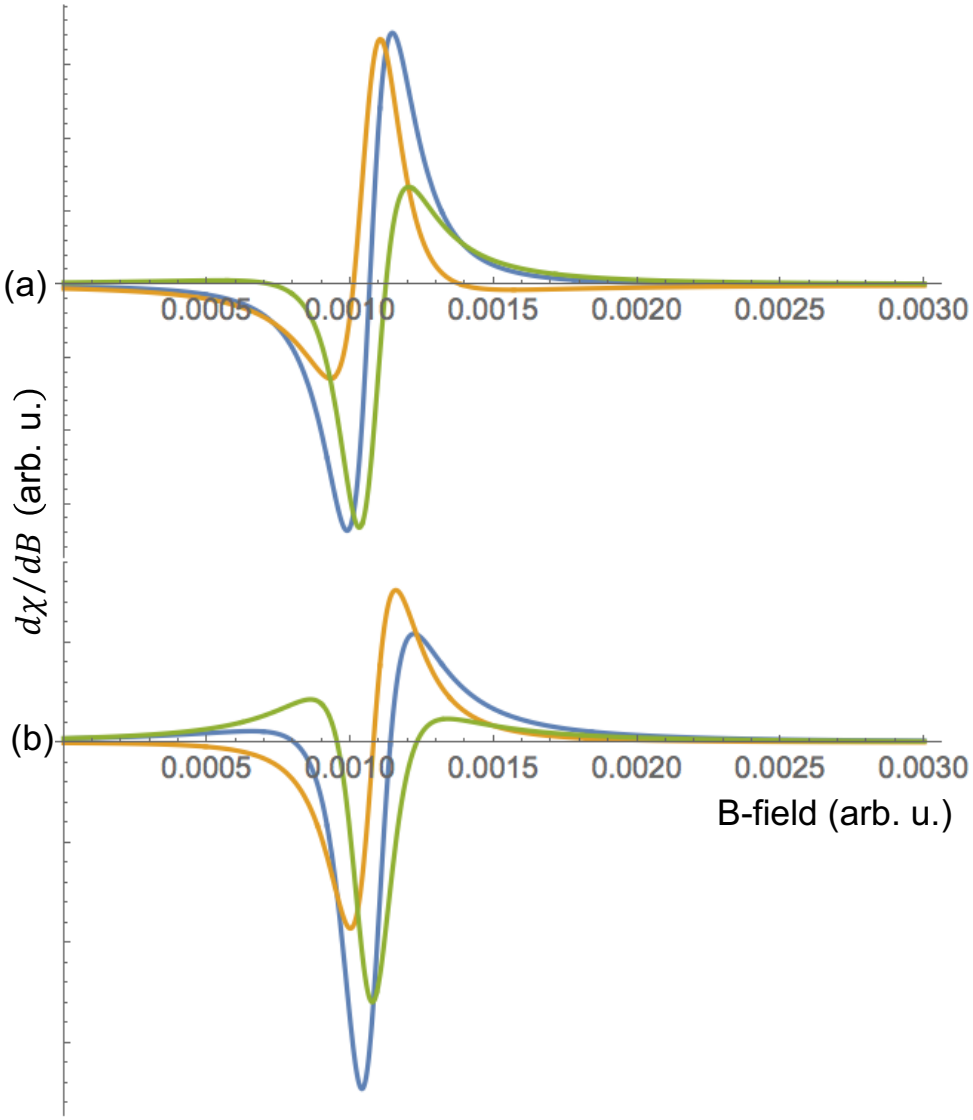

Figure 19: Shown is a calculation done with Wolfram Mathematica of $\frac{d\chi}{dB}$ in arbitrary units over the applied external magnetic field in arbitrary units as a model for a magnetite thin film. (a) The green line depicts the imaginary part χ'', the yellow line is the real part χ' and the blue line is a combination. This figure serves as an example for an asymmetric signal, arising from measuring only the dissipative part χ'' (green) by a tilted excitation field. (b) Shown are χ'' (green) and χ' (yellow). The combination of dissipative and dispersive parts of the microwave shows an asymmetric signal (blue) by tilting the angle of the excitation field and serves as an example of this line shape while measuring both contributions.

To explain the line shape of a FMR signal in a microresonator, a combination of the dissipative and dispersive part needs to be assumed. Therefore all contributions, such as inhomogeneous field distribution, tilted excitation and sample placement can be the cause for an asymmetric line shape as shown in the calculations. Those effects need to be considered when interpreting a line shape of a microFMR/EPR spectrum.

6. Dipolar Coupled Excitations in Nanoparticle Chains

6.1. Sample Preparation

For sample deposition differently diluted solutions of the bacteria in the buffer have been prepared. With the use of a micromanipulator unit, the solution has been deposited inside the microresonator. The manipulation unit was mounted under an optical microscope to deposit the sample inside the microresonator loop (see appendix A 39).

6.2. Statistically Distributed microFMR

6.2.1. microFMR on 40 Wild Type Cells

The first measurement on a reduced amount of magnetotactic bacteria has been performed on approximately 40 cells randomly orientated inside a microresonator. Figure 20 shows the FMR absorption derivative over the applied external B-field. As known from the bulk measurements the expected field range for magnetite nanoparticles is in between $225 - 375\,\mathrm{mT}$. The resonance spectrum shows a broad distribution of lines over a field range of $100\,\mathrm{mT}$. Distinct peaks are visible with line widths of $3 \pm 0.5\,\mathrm{mT}$. Those lines can be connected with single particle resonances on top of the broadened statistical distribution, resulting from dipolar coupled resonances. The random orientation of the chains and the particles create overlapping resonances result in a broad spectrum. It can be seen that the difference between the spectra at the different in-plane angles, $0\,\mathrm{deg}$ (black line) to $90\,\mathrm{deg}$ (red line), rarely differ. At a field position of $225\,\mathrm{mT}$ the $0\,\mathrm{deg}$ position shows a slight bump in the resonance. This might be attributed to a slight overall anisotropic assembly of the bacteria inside the microresonator.

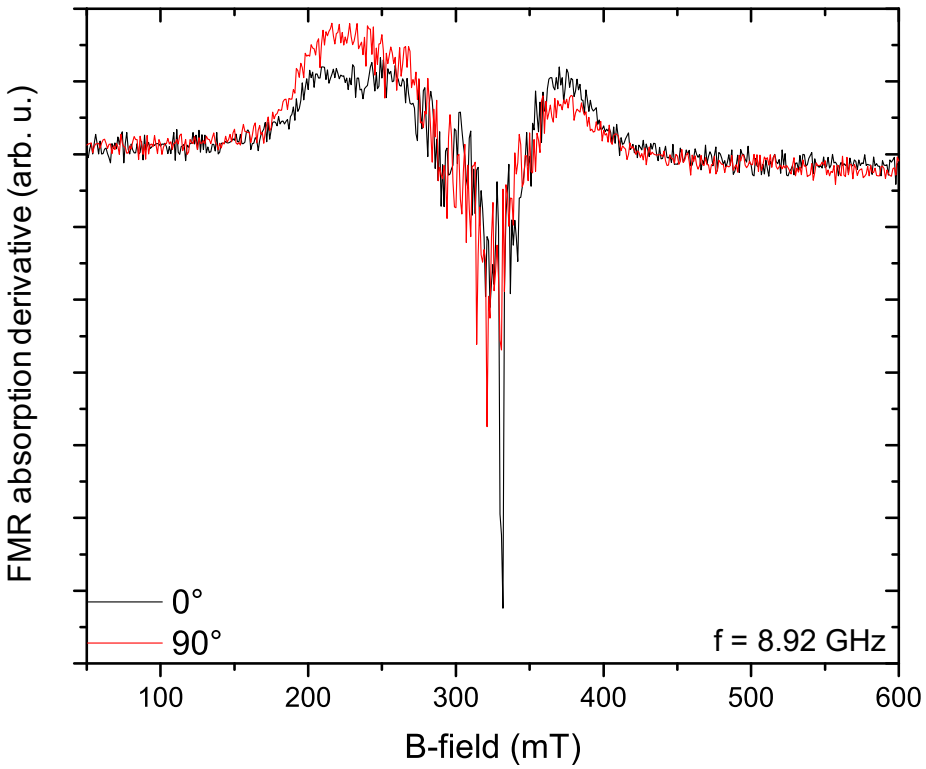

Figure 20: FMR spectrum on 40 unaligned MSR1 wild type cells inside a microresonator, the in-plane angle has been shifted from 0 deg (black line) to 90 deg (red line).

6.2.2. microFMR on 20 Wild Type Cells

To gain information on the downscaling of the particle system, a smaller amount of bacteria cells has been deposited inside the microresonator. Figure 21 shows an overview over the sample with approximately 20 cells, each with an equivalent number of nanoparticle chains. Figure 21 (a) shows an overview of the sample taken with an optical microscope. It can be seen that there are bacteria inside the microresonator loop, randomly orientated. Figure 21 (b) shows a scanning electron microscope picture with a higher magnification, verifying that the intact cells are filled with nanoparticle chains that show no anisotropic arrangement. For FMR measurements it is to be expected that a statis-

tical distribution can be seen due to the amount of nanoparticles in a range of around 400.

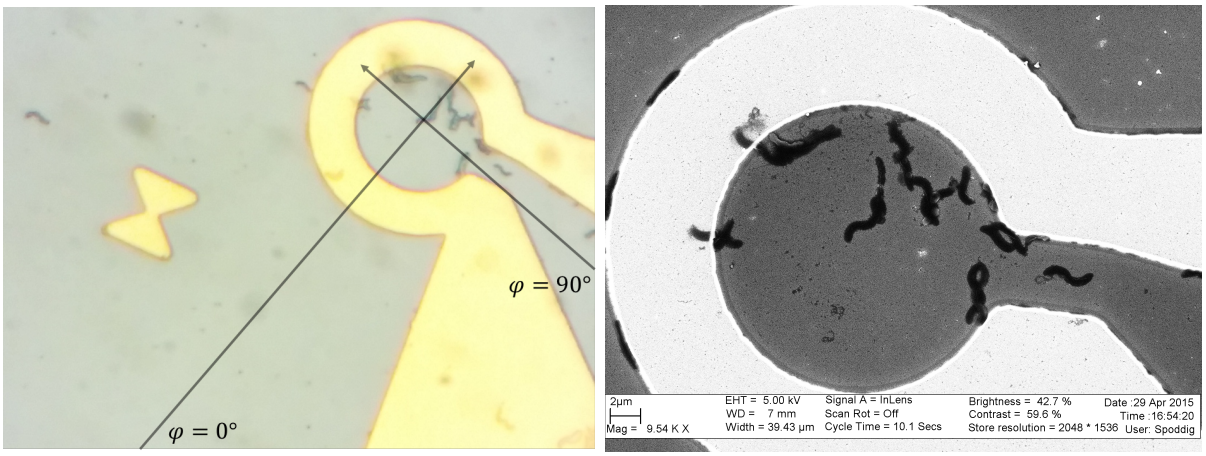

(a) optical microscope (b) SEM image

Figure 21: Pictures acquired via optical microscopy and scanning electron microscope of MSR-1 wild type bacteria. The pictures show around 20 single bacteria cells with intact cell body. Each of them contains a chain of roughly 20 nanoparticles. (a) Depicted are additionally the directions of the applied azimuthal in-plane angle during the measurement.

Figure 22 shows the FMR spectra for three different in-plane angles. The sample has been rotated in-plane by an angle of 90 deg. In the spectra it is visible that a reduction of the sample system results in distinct single particle resonances which are distinguishable from the overall statistical distribution of resonances. As in chapter 6.2.1 all the anisotropy contributions over the whole field range make up the statistical underground for the single resonances. Those result from the dipolar coupled chains in a field range from $175 - 400$ mT. The chains show a slight anisotropy in their overall distribution in the resonator as the spectrum for 90 deg shows a nearly Lorentzian line shape, while the spectrum at an in-plane angle of 0 deg flattens out at low field values. Taking into account the applied angle and sample rotation, the spectrum at 90 deg can be attributed with an easy axis of magnetization for the sample system as more particle

chains are aligned along the external magnetic field, which is also reflected in the lower resonance field values in the measurement.

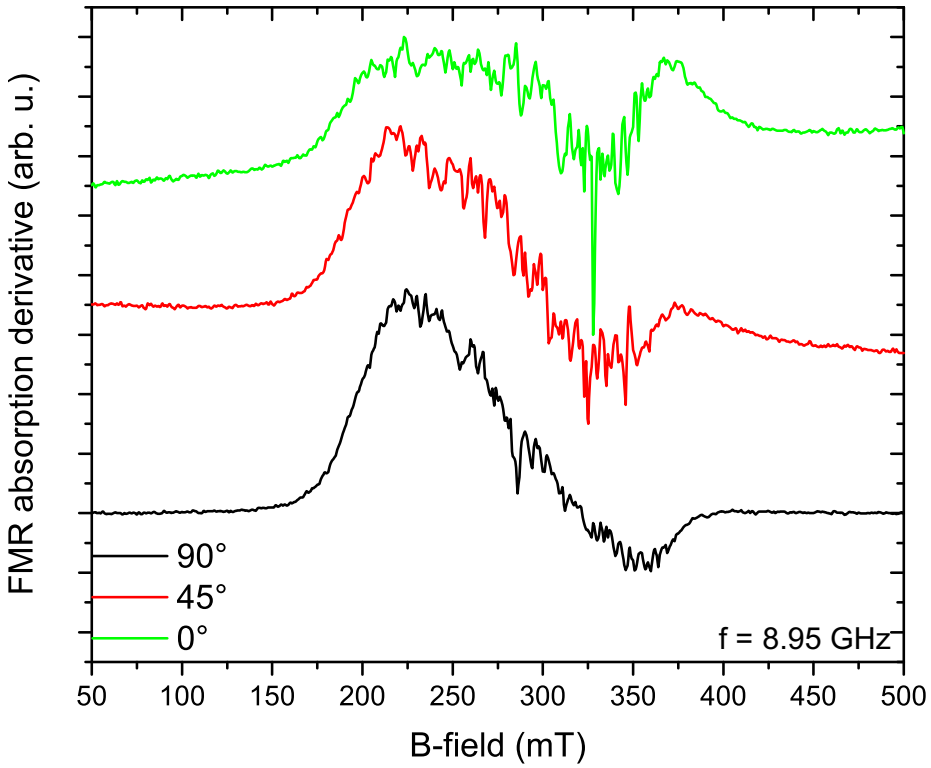

Figure 22: FMR spectrum on 20 unaligned MSR-1 wild type cells inside a microresonator. Shown lines are measured at different in-plane angles. 90 deg (black), 45 deg (red) and 0 deg (green).

6.3. Wild Type - Angular Dependent FMR

For the microFMR on a single wild type cell, a TEM carbon coated copper grid has been prepared with dried sample solution. With focussed ion beam (FIB) a lamella of the carbon layer with a single bacterium has been cut out and transferred into a microresonator. With this technique it was possible to place the sample in the middle of the loop, assuming a homogeneous magnetic field distribution for sample probing later. Figure 23 shows scanning electron microscope pictures of the resulting sample inside the resonator. The picture depicts the carbon layer with the bacterium on top of it. Inside the cell body a bent chain with 21 nanoparticles with an approximate size of $20 \pm 5\,\mathrm{nm}^3$ can be seen. The chain exhibits slight distortions in the particle spacing as well as in particle size.

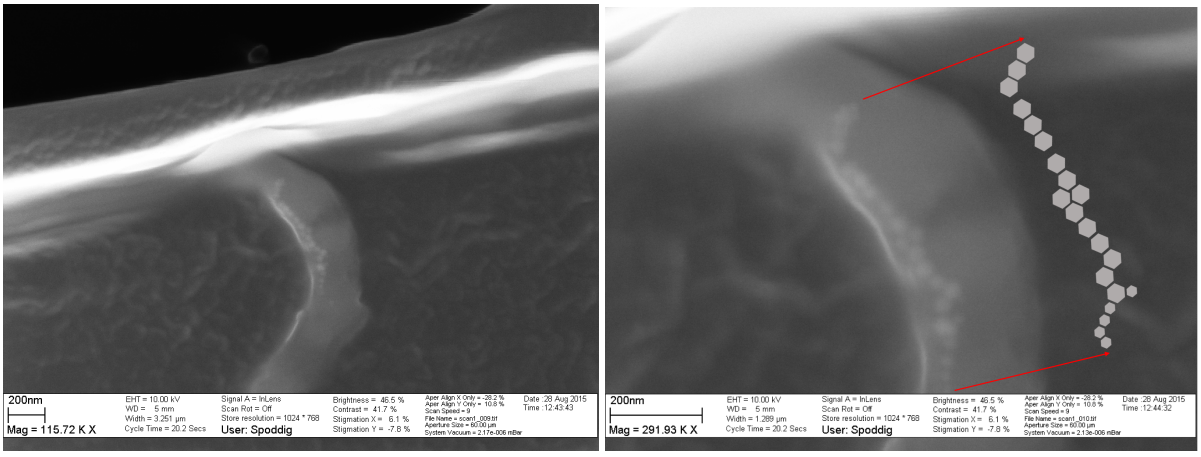

(a) (b)

Figure 23: (a) Scanning Electron Microscope image of MSR1 wild type bacterium on a TEM carbon layer, deposited inside a microresonator via focussed ion beam technique (FIB) showing 21 single particles arranged in a bent chain (b) higher magnification of the chain itself, the inset shows a 2 dimensional representation of the particle chain to visualize the possible particle arrangement.

Figure 24 shows the FMR spectra on the single cell sample for three different in-plane angles. It can be seen that there are single resonances which shift with the applied

in-plane angle. The resonance positions are reproducible and shift with the applied azimuthal in-plane angle. Yet, the spectrum at an in-plane angle of 0 deg has a very low intensity. A possible explanation will be given when discussing the full angle dependent spectrum.

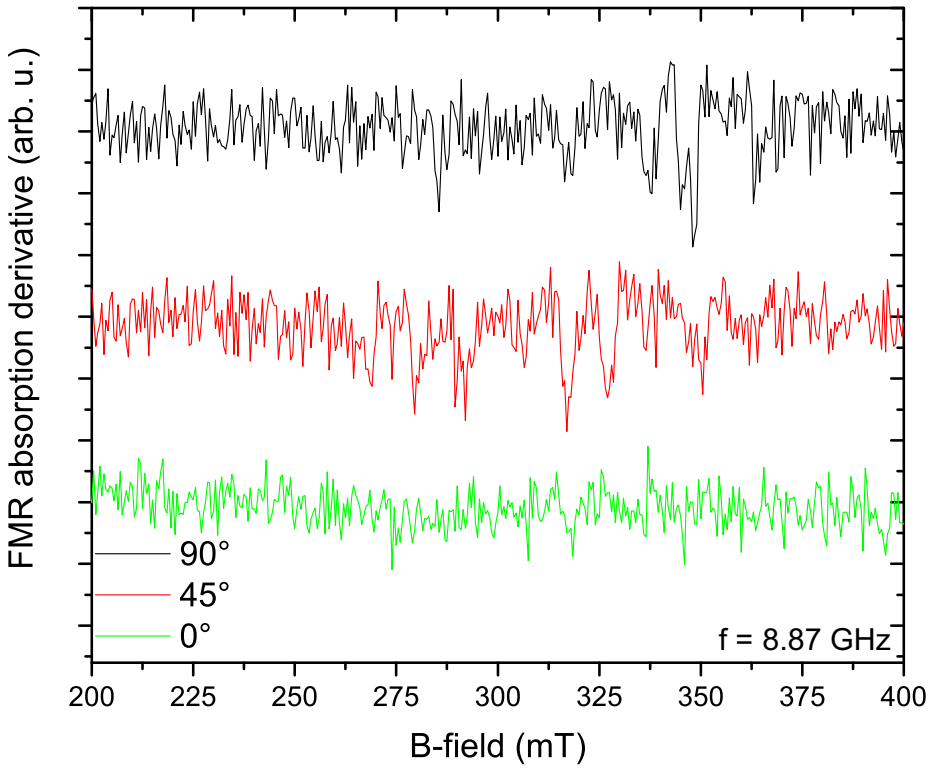

Figure 24: FMR spectrum on a single MSR-1 wild type cells inside a microresonator at three different in-plane angles φ from 90 deg (black), 45 deg (red) and 0 deg (green).

To gain more information on the intrinsic anisotropies, the single cell sample has been measured with full angle dependence. Figure 25 shows the amplitude plot (min to max) of the FMR absorption derivative as a function of the applied external magnetic field over the azimuthal in-plane angle φ. At a field position of 318 ± 0.5 mT an EPR signal can be seen, which does not show any anisotropic behavior. This line can be

attributed again to the HEPES buffer. Possible reasons for this signal are described in chapter A.5. The greyscale plot clearly shows distinct modes in a field range of $220 - 375\,\mathrm{mT}$, exhibiting a uniaxial anisotropy. The most pronounced has the highest intensity and has its minimum at $-20\,\mathrm{deg}$. Taking into account the sample placement and the installation of the sample inside the setup (see Figure 26), the chain of particles here was aligned in direction of the external magnetic field, which can be attributed to its easy axis of magnetization along the chain. However, the main mode shows breaks along its downward path to its energetic minimum. Considering the particle arrangement it can be assumed, that, coming from an angle which is attributed with the hard axis of magnetization and due to the bent chain, different parts of the chain come into resonance one after another. Furthermore, weaker modes are visible at higher field values which match with simulations done and will be discussed in chapter 6.5. To explain the breaks on the downward branch it has to be taken into account that the geometry of the particle chain contributes strongly. As the angle shifts, different chain parts are energetically preferred leading to a step wise behavior on the downward branch. Another possible reason for the breaks in the mode, a tilted microwave excitation, will be addressed in chapter 6.5. In the energetic minimum at an in-plane angle of $-20\,\mathrm{deg}$, the resonance are strongly suppressed and not visible. This might be attributed to two parts of the chain whose spinwave excitations oscillate with an opposite sign and result in a vanishing signal. On the upward branch, a uniform mode again energetically is preferred as the sample starts with its easy axis. Breaks in the excitation modes cannot be seen. The fact that a nearly uniform excitation mode with uniaxial anisotropy can be seen suggests that the nanoparticles inside the chain are strongly coupled due to their longreaching dipolar interactions and a spinwave is excited over the interparticle gap of approximately $10\,\mathrm{nm}$. At an azimuthal angle of $45\,\mathrm{deg}$ a crossing of modes is visible. This phenomenon fits with performed simulations and will be discussed furthermore in detail in chapter 6.5. For a better understanding of a possible particle arrangement and the resulting stepwise resonances, a model of the particles and possible ordering of the particles to each other is shown in Figure 26.

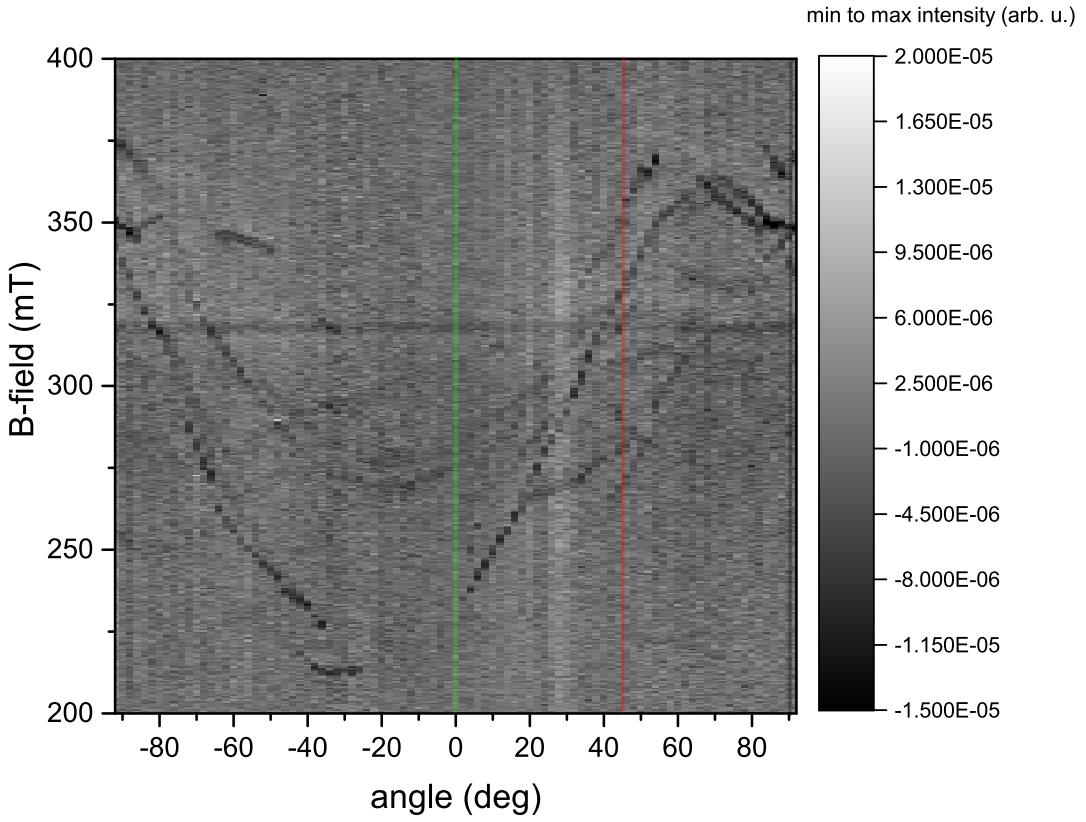

Figure 25: Angular dependent amplitude plot of one wild type MSR-1 cell measured in a microresonator. The grayscale plot depicts the minimum and maximum amplitude of the resonances. The x-axis shows the applied in-plane angle φ over the applied external magnetic field. The green, red and black line indicate the positions of the spectra shown in Figure 24. The measurement direction started at -92 deg and the angle was rotated in-plane up to $+92$ deg.

For easier depiction, the particles are represented as a 2 dimensional projection, here shown as a hexagonal structure. The real crystal morphology and crystallographic facets hereby are neglected. The facets facing each other are not to be mistaken with real crystallographic planes. Shown are differently sized particles and the bent chain as well as a double occupied chain position roughly in the middle of the chain. Figure 26 shows

the position of the nanoparticle chain with respect to the azimuthal in-plane angle of the external magnetic field during the measurement.

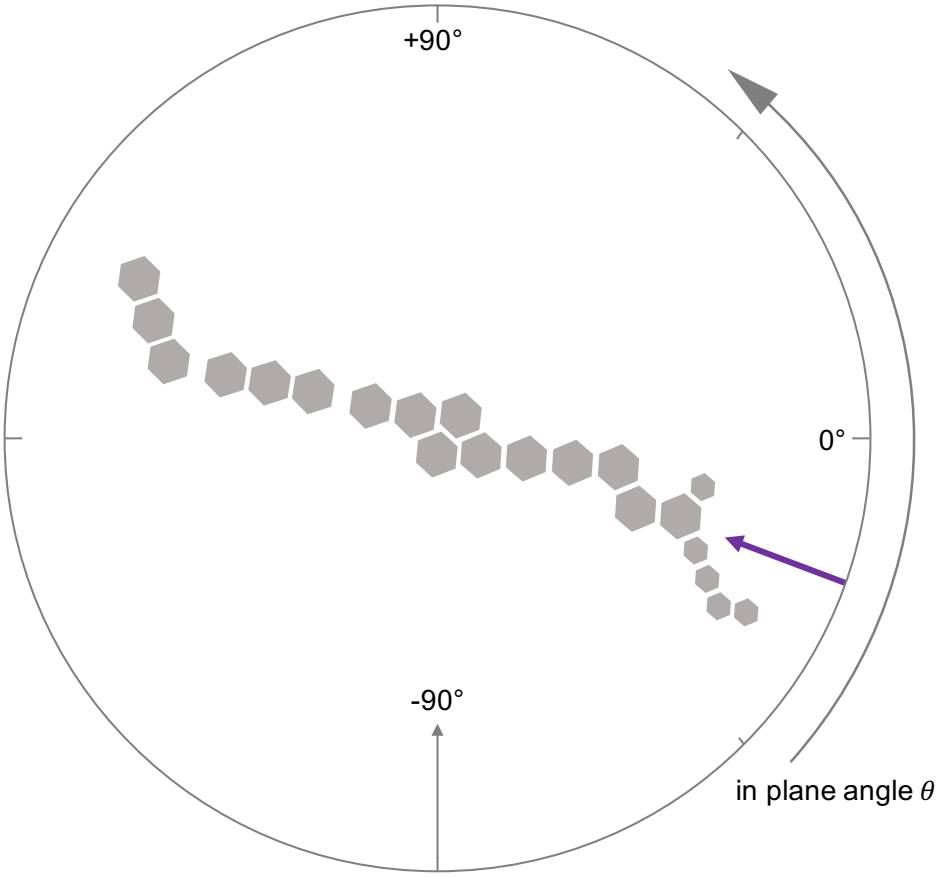

Figure 26: Schematic representation of the magnetite nanoparticle chain inside the bacterium, deposited inside the microresonator with FIB. The chain is pictured with respect to the in-plane angle φ. Measurements have been performed from $-92\,\mathrm{deg}$ to $+92\,\mathrm{deg}$. The purple arrow shows the direction of the easy axis for the nanoparticle system at approximately $-20\,\mathrm{deg}$.

6.4. △ Mamk - Angular Dependent FMR

After evaluating a chain which roughly can be described as uniaxial, a measurement has been performed on two single nanoparticle chains, exhibiting different geometries. The bacteria placed in the microresonator were mutant MSR-1 bacteria, $\Delta Mamk$. Figure 27 shows an scanning electron microscope image of the bacteria cells inside the microresonator, the inset depicts the two nanoparticle chains. Despite the two cells which are located close to the resonator edge, there are no cells inside the resonant structure. Considering the cell location, the assumed line shape which has been discussed in chapter 5.2, needs to be taken into account as the cells are most likely placed in a B-field inhomogenity. The bacteria cells have been deposited in the resonator with help of a micromanipulator unit.

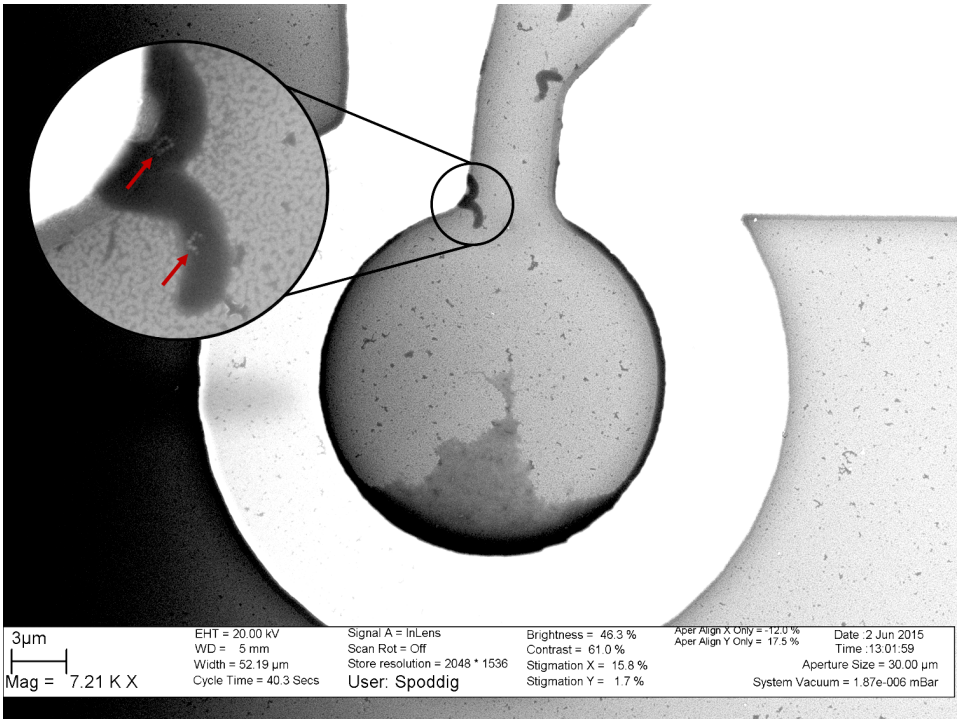

Figure 27: Scanning electron microscope image of the intact bacteria cells with encapsulated nanoparticle chains, the inset shows the chains at a higher magnification. The red arrows in the inset mark the particle chain position.

Figure 28 shows a schematic representation of a 2D model of the measured chains. The first chain is U-shaped and consists of 9 single particles. The second chain consists of 7 particles and has the morphology of an deformed c and will be addressed as c-shape. All the particles are in a size range of around $(20-30\,\mathrm{nm})^3$. From the crystalline anisotropy and the symmetry of the geometrical arrangement of the chains, a fourfold anisotropy due to the particle arrangement should be visible in the angle dependent spectrum from both the u-shape as well as the c-shape. Additionally a twofold anisotropy can be expected from the u-shape with an easy axis along the the two arms consisting of each 4 particles.

Figure 28: Schematic 2D representation of the magnetite nanoparticle chains inside the two $\Delta Mamk$ bacteria inside the microresonator. The model does not display the real particle shape or the real spacing between the two chains to each other and only serves as a guide to the eye.

Figure 29 shows the average of 80 single FMR spectra at three different azimuthal angles. The spectrum shows the FMR absorption derivative over the applied external magnetic field. Due to the averaging the noise has been cancelled out and led to a signal to noise ratio of 10:1. Resonances can be seen in a field range of $275-375\,\mathrm{mT}$, lying in the expected field range for magnetite. Almost separable lines make it possible to

observe line shapes and line widths of $3 \pm 0.5\,\mathrm{mT}$. It can be seen, that the resonances shift with the applied in-plane angle. To evaluate the anisotropies in detail, a full angle dependent measurement has ben performed on the given sample.

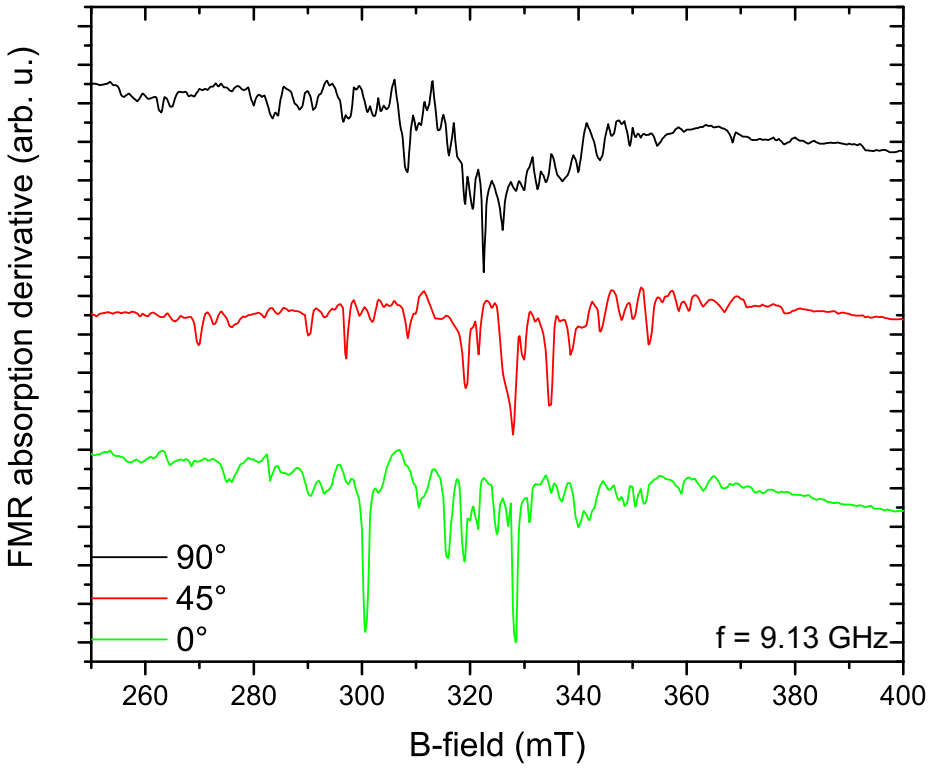

Figure 29: FMR spectrum on two nanoparticle chains of $\Delta Mamk$ bacteria cells inside a microresonator. Shown are the averages of 80 spectra of different in-plane angles. The plot shows the amplitude of the FMR absorption derivative over the applied external magnetic field. Measured in-plane angles are 90 deg (black), 45 deg (red) and 0 deg (green) with a signal to noise ratio of 10:1.

Figure 30 shows the amplitude plot of the absorbed FMR derivative (grayscale from min to max) as a function of the applied external magnetic field over the azimuthal in-plane angle φ. The signal is in the same field range as observed for the bulk measure-

ments, $225 - 375\,\mathrm{mT}$. Depicted as a black dotted line, a distinct fourfold anisotropy is visible, arising from the chain arrangement of the particles as the angle increases.

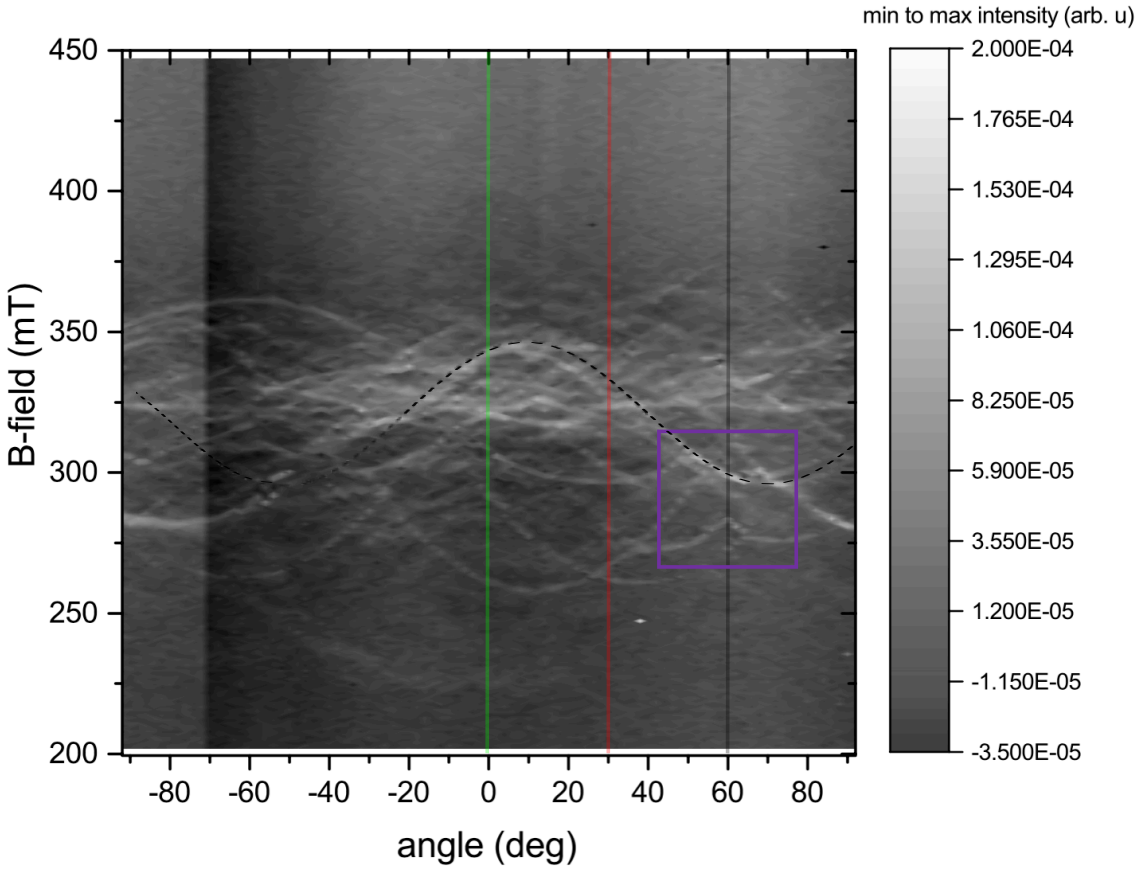

Figure 30: Amplitude plot of two chains of nanoparticles produced by $\Delta Mamk$ bacteria measured in a microresonator. The grayscale plot depicts the minimum and maximum amplitude of the resonances obtained. The x-axis shows the applied in-plane angle φ over the applied external magnetic field. The green, red and black line indicate the spectra shown in Figure 32. The dotted line shows a calculated fourfold anisotropy and the purple square indicated the position of repulsive modes, as depicted in Fig. 31.

Furthermore coupled modes can be distinct from the single resonances. The nanoparticles inside the chains exhibit long range dipolar interactions. Therefore it can be concluded, that there are dipolar coupled excitation modes throughout them. The u-shape and the c-shape of the chain assemblies lead to a coupling of modes which do not cross while being rotated. At a field position of 280 mT and an in-plane angle of 60 deg as well as at a field position of 300 mT at an corresponding angle of 70 deg those repulsive modes can be seen as depicted in Figure 31.

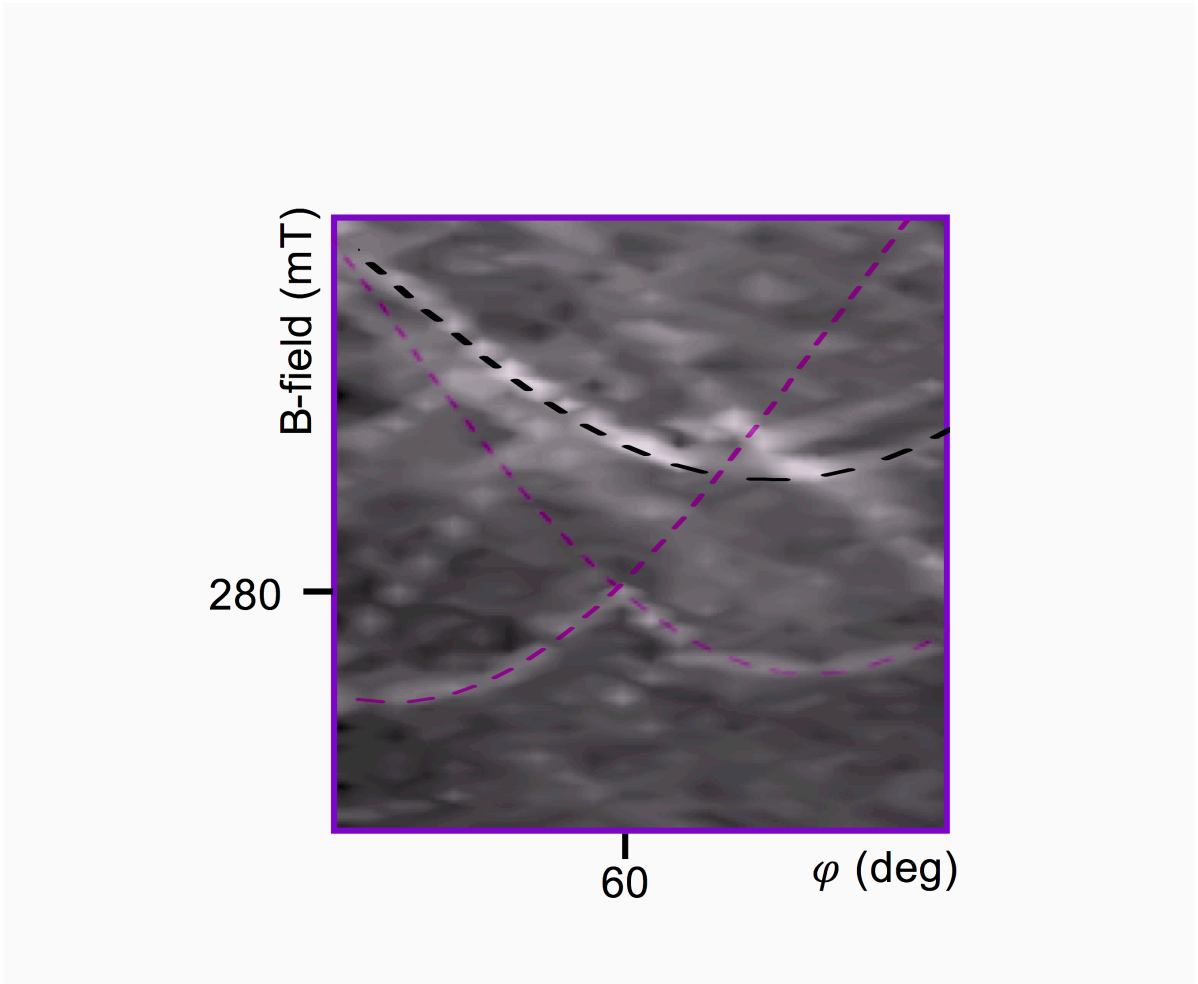

Figure 31: Magnification of the repulsive modes at a field position of 280 mT and an in-plane angle of 60 deg from the amplitude plot depicted in Figure 30. The dotted purple line shows two calculated fourfold anisotropies that do not cross. The dotted black line depicts another fourfold anisotropy.

The first mode is energetically preferred, because the external magnetic field is aligned along an easy axis of magnetization, the other part of the chain is aligned along its hard axis. During the sample rotation the mode from the second chain part is energetically preferred and the modes do not cross.

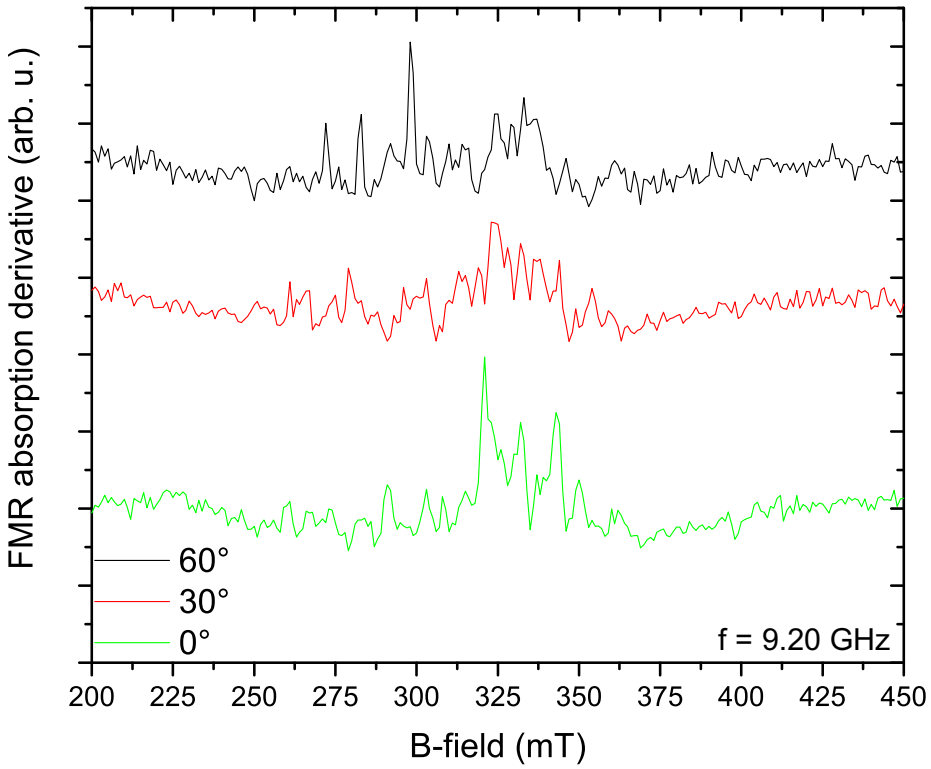

Figure 32: FMR spectrum on two $\Delta Mamk$ cells inside a microresonator. The plot shows the amplitude of the FMR absorption derivative over the applied external magnetic field. Measured in-plane angles are 60 deg (black), 30 deg (red) and 0 deg (green)

In the microFMR measurements of countable nanoparticle numbers, the line shape shows the same features as described in chapter 5.2. Especially the placement of the $\Delta Mamk$ bacteria in the resonator are at the loop edges, assuming that the measurement takes place in a regime where the exciting microwaves are not completely perpen-

dicular to the external magnetic field, influencing the shape strongly. From the angle dependent measurement a crystalline anisotropy field $\frac{K_4}{M} = 29 \pm 3\,\mathrm{mT}$ for the different single particles could be extracted. It is in the same order of magnitude as bulk magnetite [Bic50] [K§9] and fits the values assumed for statistical fittings of magnetotactic bacteria. The typical resonance of a single particle linewidth is $3 \pm 0.5\,\mathrm{mT}$. This value is roughly five times smaller than epitaxially grown magnetite thin films [Bra08] but in the area of single crystalline iron thin films [Hei93].

6.5. Discussion of Single Cell Measurements

In order to evaluate the data further more, simulations for different particle arrangements, resembling the single cells, have been done. To simulate the magnetic behavior inside single nanoparticle chains and arrangements, first a micromagnetic simulation with OOMMF (Object Oriented MicroMagnetic Framework) [Don] [Sch14] has been performed on a simple geometry. Figure 33 shows an OOMMF simulation of a nanoparticle chain, consisting of five cubic magnetite particles with an edge length of 30 nm and a spacing in between them of 10 nm. Shown is an amplitude plot from minimum to maximum FMR absorption signal amplitude over the applied external magnetic field. The amplitude plot is given for different in-plane angles. The plot shows three different modes in a field range, corresponding to the actual experiments done. A main mode with uniaxial anisotropy is visible and has the biggest intensity. Furthermore there are two weaker modes at higher field values. Those modes can be attributed to a mode arising from the boundary particles and the second from incoherent excitation between the particles. The modes cross at an in-plane angle of 65 deg. This spectrum can be compared to the single chain measurement in chapter 6.3. The wild type chain in the bacterium exhibits a mainly uniaxial anisotropy due to its geometrical arrangement and shows additional weaker modes at higher field values as well. Furthermore crossing of modes is visible at an azimuthal in-plane angle of 45 deg, as the easy axis of magnetization here is at an angle of −20 deg. Thus, it can be assumed that the main mode with

high intensity arises from the uniaxial anisotropy of the chain, and the weaker modes from boundary conditions in the system.

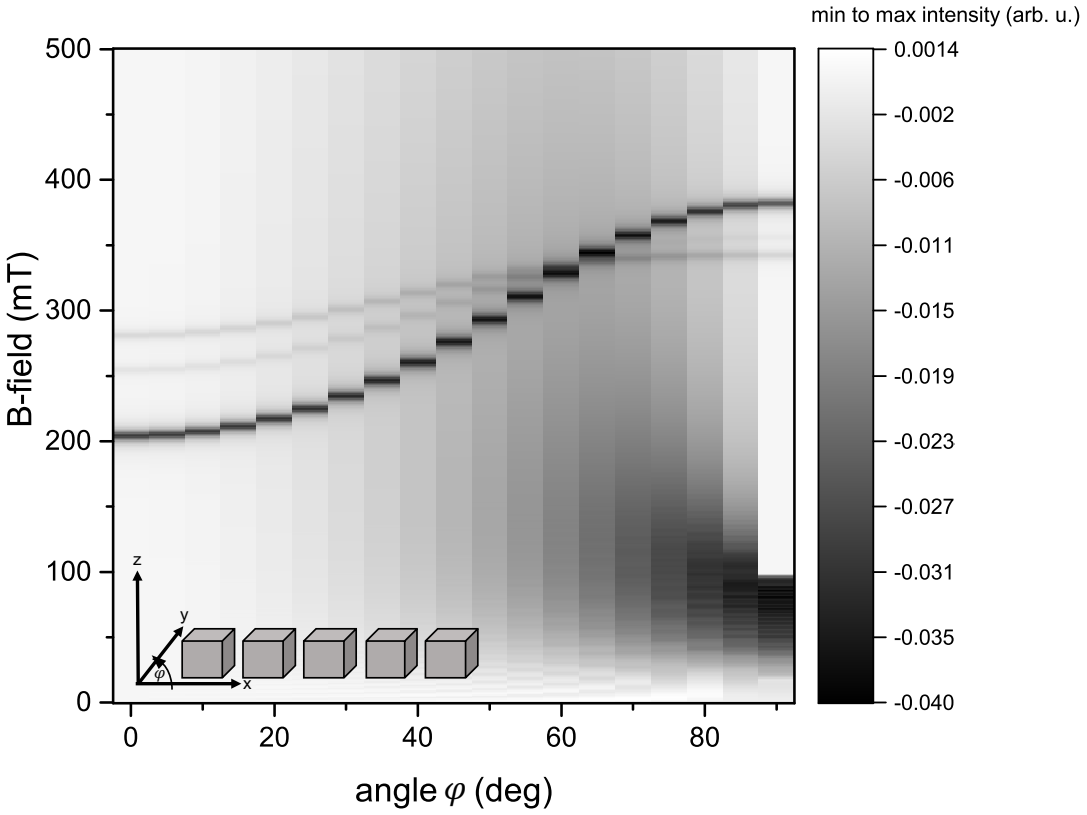

Figure 33: amplitude plot (min to max) of the azimuthal in-plane angle φ in the sample plane over the applied external magnetic field as calculated with OOMMF. The simulation was modeled for chain of 5 nanoparticles with interparticle distance of 10 nm. Parameters can be found in chapter A.3. The inset shows a model of the assumed sample geometry and arrangement. Data processed by C. Derricks.

The calculations done show, that the system is strongly dipolar coupled. To visualize the stray fields arising from the sample system, it has been calculated using MuMax^3 [Van14]. Figure 34 shows the model of the particle arrangement used for the simulations

as acquired in SEM measurements. The nanoparticles have been modeled as truncated cubes with their easy axis, [111], along their body diagonal and an edge length of 27 nm.

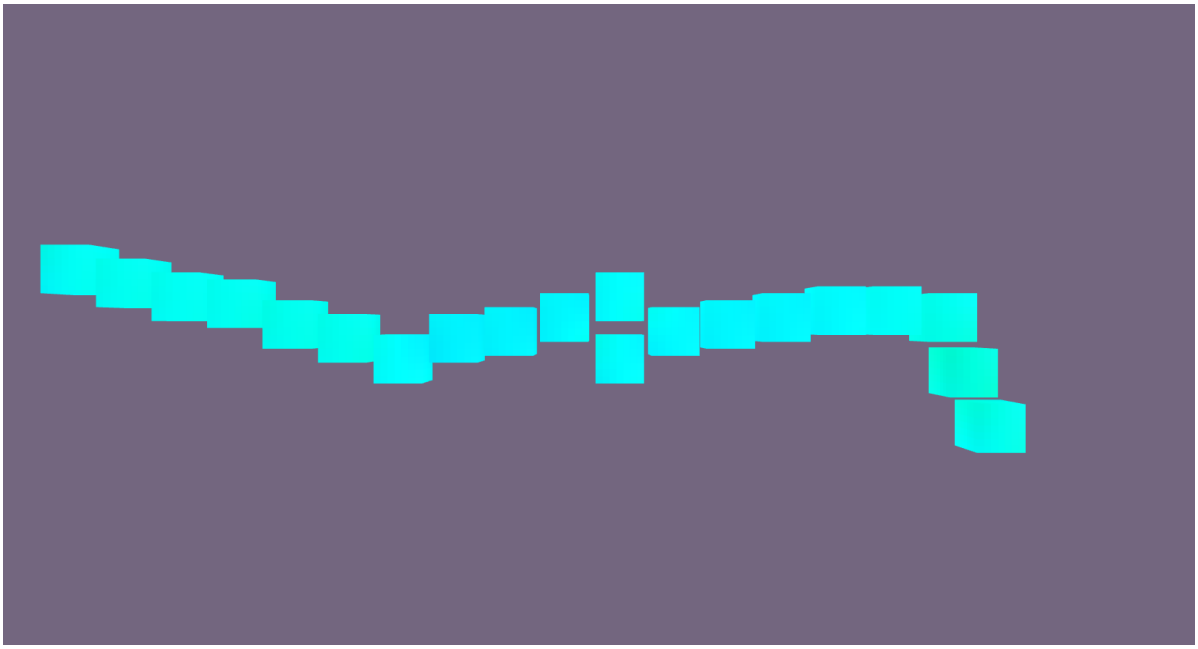

Figure 34: Model of truncated cubic particles (size $(27\,\mathrm{nm})^3$) used for MuMax^3 simulations, data proceccing by T. Feggeler.

The obtained stray field distribution is plotted in Figure 35. The streamline plot shows strong dipolar coupling between the single particles as well as longreaching coupling throughout the whole chain. Assuming strong dipolar coupling it is possible to explain the coupled excitation modes measured in the full angle dependence of both the wild type single cell, as well as the two mutated cells. The estimated demagnetization field could be quantified by the simulations done. Its values are in the range of $50 - 70\,\mathrm{mT}$ in between the particles.

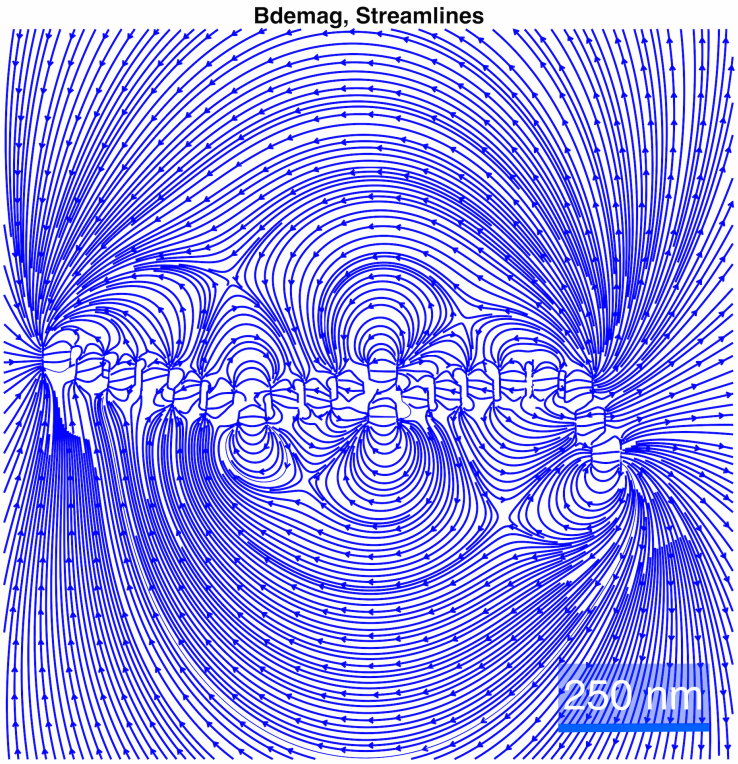

Figure 35: Streamline plot of demagnetization field inside the particle chain, data processing by T. Feggeler. Particle size: $(27\,\mathrm{nm})^3$ with truncated edges, $M_\mathrm{S} = 4.72 \cdot 10^5\,\frac{\mathrm{A}}{\mathrm{m}}$, $K_4 = -1.1 \cdot 10^4\,\frac{\mathrm{J}}{\mathrm{m}^3}$, $g = 2.12$

Next to multiple excitation modes, the experimental data on the single nanoparticle chain shows breaks on the downward branch coming from a hard axis of magnetization (see Fig. 25). This either can be attributed to the bent geometry of the particle chains as described in chapter 6.3 or a tilted microwave excitation. To visualize the effect of a tilted microwave excitation, numerical calculations have been performed on an iron thin film with an out-of-plane hf-microwave tilt of $\pm 5\,\mathrm{deg}$. Figure 36 shows an intensity plot of the microwave absorption χ''. By tilting the angle, the out of plane angular dependence shows the same behavior of a broken mode.

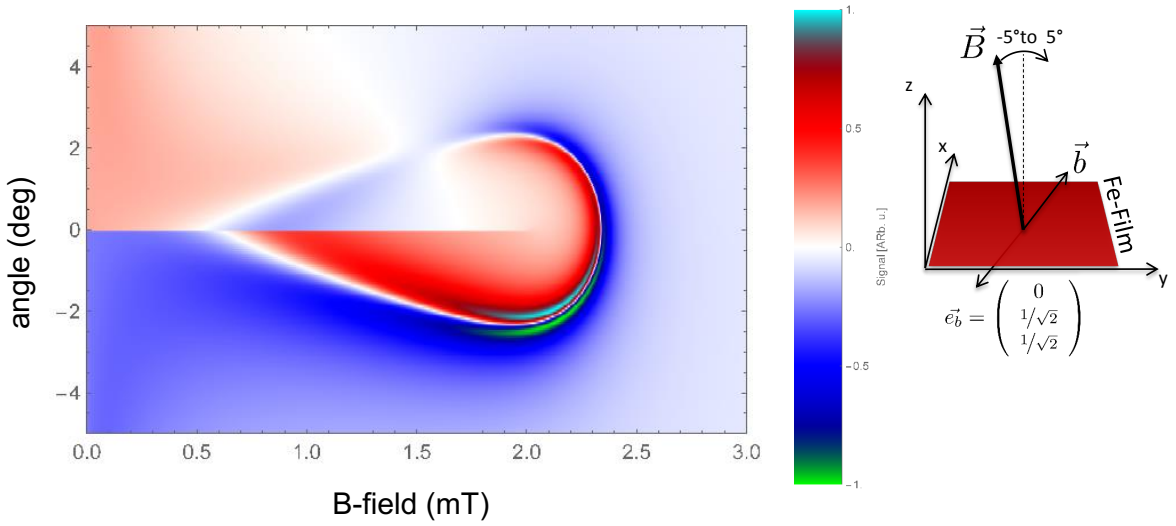

Figure 36: Calculation of the angle dependent spectrum of an iron thin film ($d = 10\,\mathrm{nm}$) with tilted microwave excitation of $f = 9.3\,\mathrm{GHz}$ as an intensity plot (turquoise maximum, green minimum). The parameters used are $M_\mathrm{S} = 1.7 \cdot 10^6\,\frac{\mathrm{A}}{\mathrm{m}}$, $K_4 = 5 \cdot 10^4\,\frac{\mathrm{J}}{\mathrm{m}^3}$, $K_\mathrm{surface} = 5.5 \cdot 10^{-4}\,\frac{\mathrm{J}}{\mathrm{m}^3}$, $\alpha = 0.0045$, $g = 2.1$. the right part shows a schematic picture of the film with the applied external magnetic field and microwave excitation. Calculation courtesy of B. W. Zingsem.

This effect has been measured in [Mec97]. Figure 37 shows an amplitude plot of the angle dependent FMR measurement of an iron thin film with a thickness of 20 nm. The polar angle ϑ was tilted from in-plane to out-of-plane. The plot shows a break in the excitation mode while measuring from the magnetic hard direction to an easy one ($-1.75\,\mathrm{deg}$). This behavior is consistent with the performed calculations done (see Fig. 36) and the experimentally observed behavior inside the single nanoparticle chain.

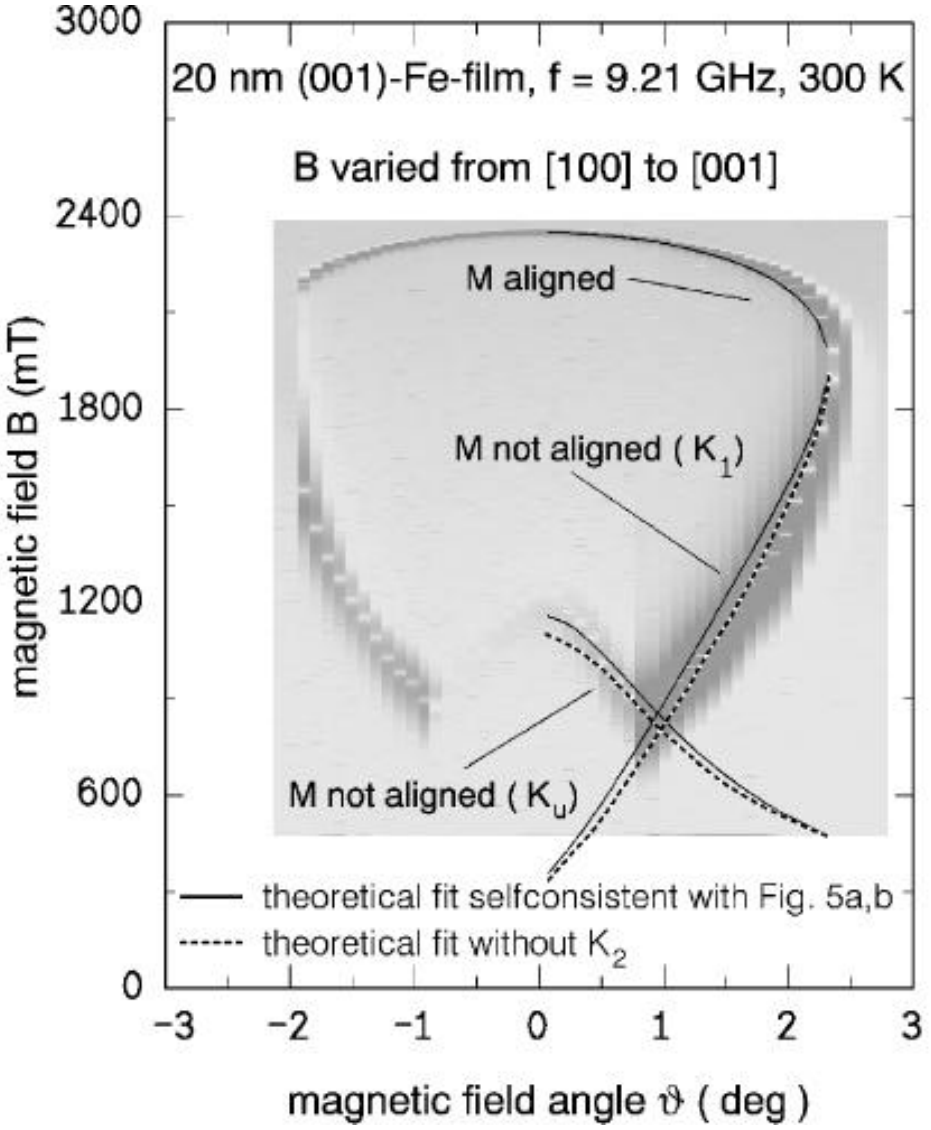

Figure 37: Amplitude plot of the angular dependent resonance positions of a 20 nm iron thin film. The angle has been tilted from in-plane to out-of-plane. The signal intensity is shown from minimal (white) to maximal (black) amplitudes. Picture taken from [Mec97].

In the energetic minimum of the single cell measurement (see Fig. 25) at an external magnetic field of 220 mT and an in-plane angle of 60 deg, the mode vanishes. At this field value, the chain is aligned along its easy axis of magnetization. Due to the particle arrangement and the chain geometry we can assume higher modes of a higher order which

are energetically preferred. With the use of MuMax[3] a more simplified particle geometry as in Figure 34 has been used. The FMR frequency spectrum at a static external B-field at 220 mT has been deduced by a Fast Fourier Transform (FFT) of the magnetization relaxation [Mec08]. The magnetization here is deflected out of its equilibrium position with an external magnetic field in the range of the microwave excitation. Switching off the deflection field leads to a precession of the magnetization into its equilibrium position. With a FFT the spectrum as seen in Figure 38 is obtained. It shows the resonance frequencies for the particle assembly. Visible are three modes, with the main uniform excitation mode at a frequency of $f = 10.9$ GHz and two spin wave excitations. The mode next to the uniform excitation mode can be attributed to the oscillating excitation with $\vec{k} = 2$ as shown in the inset of Fig. 38.

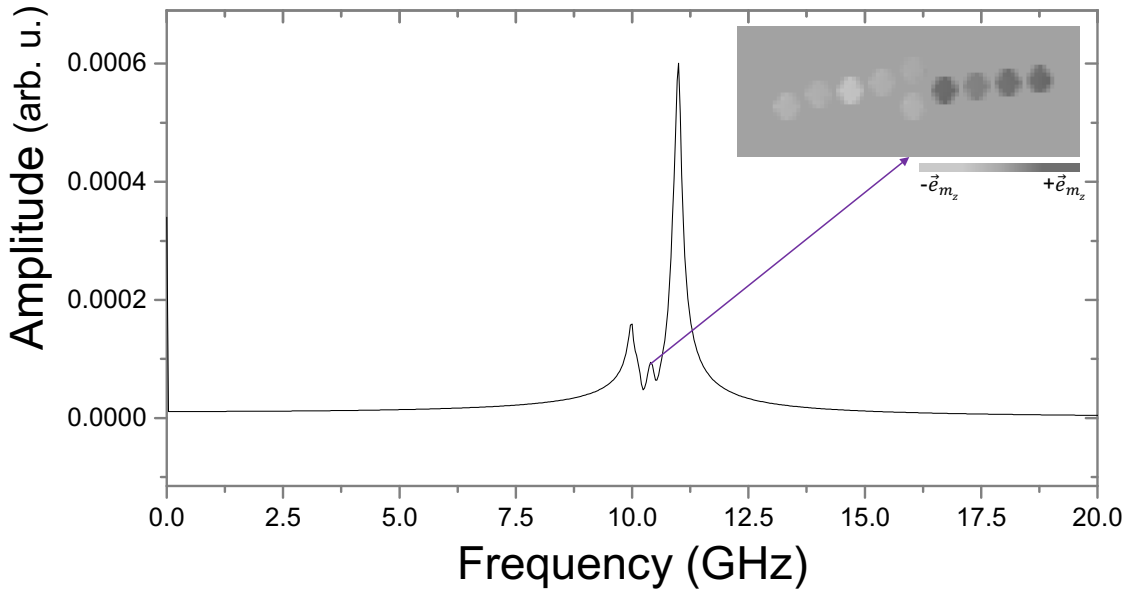

Figure 38: Fast Fourier Transform of the magnetization relaxation at a static external field of 220 mT. The inset shows the assumed geometry of the reduced nanoparticle chain as well as the direction of the $\vec{e}_{m_z}$ component (light grey = -1; dark grey = +1). The opposing chain parts oscillate with an opposite sign.

Therefore there is no resonance visible in the measured spectrum along the easy axis of magnetization because of its weak intensity which lies in the range of noise of the setup. More than three modes are not visible in this calculation because the simplified assumed sample geometry (see inset Figure 38) does not allow more modes than $\vec{k} = 3$.

7. Conclusion and Outlook

In this work it was possible to measure a single cell of a magnetotactic bacterium of the strain *Magnetospirillum Gryphiswaldense* with a single nanoparticle chain. This chain consists of 21 particles in a size range of $(20 - 30\,\mathrm{nm})^3$. Through the strongly dipolar coupled system with demagnetization fields in between the particles of $50 - 70\,\mathrm{mT}$, the magnetic characteristics of dipolar coupled magnetite nanoparticles could be observed. Measurements on different geometrical arrangements of nanoparticle chains, such as a u-shape (9 particles) and a c-shape (7 particles) have been measured with full angle dependence to evaluate the anisotropic behavior. It could be experimentally shown that different particle geometries exhibit dipolar coupled spinwave excitations. Repulsive modes could be set apart from uniform excitations in the symmetrically arranged u- and c-shaped particle chains. In the single cell wild type measurement an overall uniaxial anisotropy dominates, yet weaker modes from the chain boundaries, the end particles, as well as incoherent excitations between the particles are visible. Micromagnetic simulations and calculations have been performed in order to verify the measured data. The calculations done show a similar behavior even though simplified models for the particle assemblies were assumed. From the measurements a crystalline anisotropy field for single magnetite nanoparticles could be extracted with a value of $\frac{K_4}{M} = 29 \pm 3\,\mathrm{mT}$. This value lies in the range of single crystalline bulk magnetite [Bic50]. The extracted line width at X-band frequencies for a single crystalline magnetite particles of a size of $(20 - 30\,\mathrm{nm})^3$ could be estimated with $3 \pm 0.5\,\mathrm{mT}$. This value is five times smaller than the line width for epitaxially grown magnetite thin films [Bra08] but in the range of single crystalline iron thin films [Hei93].

For a further understanding of the sample system, more micromagnetic calculations are in progress. Additionally the experimental analysis of other particle configurations would give more information on the coupling mechanisms in nanoparticle arrangements. Especially Scanning Transmission x-ray microscope FMR could be a useful tool to evaluate the influence of single particles on an ensemble.

A. Appendix

A.1. Sample Preparation with Micromanipulator Unit

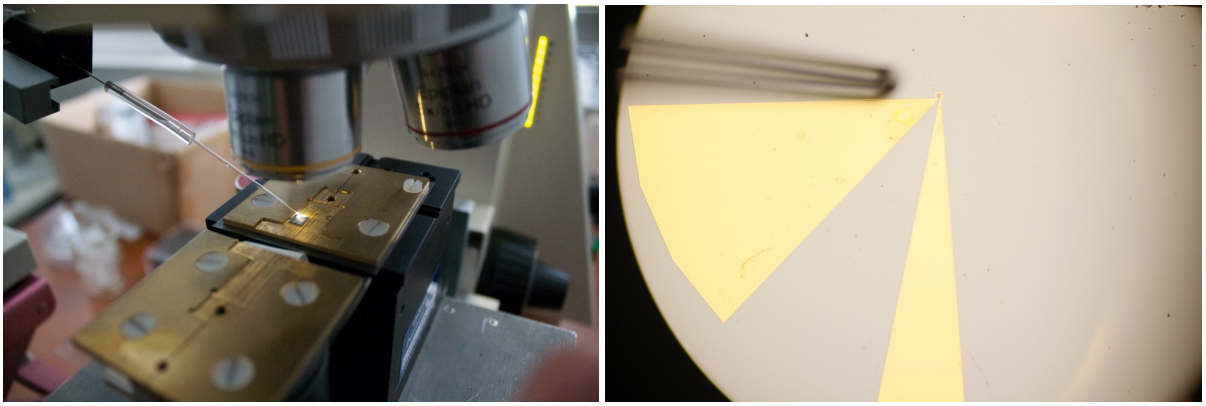

(a) Setup of micromanipulator under the microscope

(b) View through the ocular with manipulator tip visible left of the microresonator loop

Figure 39: Setup of the micromanipulator unit used for sample preparations in this work.

A.2. FMR Measurement Parameters

Sample	f [GHz]	f_{mod} [Hz]	modulation [G]	t_{const} [ms]	power [mW]
wt bulk	9.51	777.77	2	1000	10
$\Delta Mamk$ bulk	9.51	777.77	2	1000	10
40 cells wt	8.92	123.45	1.8	300	32
20 cells wt	8.95	123.45	1.8	300	13
single cell wt	8.87	123.45	1.8	1000	50
$\Delta Mamk$ 2 cells	9.2	123.45	1.8	300	47

Table 2: Overview of the used measurement parameters for FMR experiments in this work. All measurements have been performed at 18 dB/okt.

A.3. OOMMF Parameters

Parameter	Name	Value
width (x)		30 nm
length (y)		30 nm
height (z)		30 nm
gap size	spacernm	10 nm
number of particles		5
cell size (x)	cellsizenm	5 nm
cell size (y)	cellsizenm	5 nm
cell size (z)	cellsizenm	5 nm
$\mu_0 H_x$	Bx1, Bx2	500 mT => 0 mT
$\mu_0 H_y$	By1, By2	0 mT
$\mu_0 H_z$	Bz1, Bz2	0 mT
colatitude field angle	colfielddeg	90
azimuthal field angle	azifielddeg	**0 – 90, (stepsize 5)**
field step size $\mu_0 \Delta H_x$	fieldsteps	1 mT
exchange constant	A	1.32×10^{-11} J/m
wave function		sinus
microwave frequency	fre	9.433185 GHz
microwave amplitude	amp	250 µT (198.94 A/m)
oscillations	osc	100
Landéfactor	gfact	2.05
cubic anisotropy (first order)	K1kJm3	-4
damping (Gilbert)	alpha	0.01
magnetization	Ms	4.8×10^5 A/m
maximum time step size	max_timestep	10^{-12} s
minimum time step size	min_timestep	
stopping time	stopping_dm_dt	osc/fre

Figure 40: Parameters used for micromagnetic simulations done for a nanoparticle chain consisting of 5 nanocubes with an edge length of 30 nm and interparticle distance of 10 nm. Courtesy of C. Derricks.

A.4. Exemplary MuMax^3 Script

```
//HF parameter:
f := 9.208e9 // 9GHz Frequency
Am := 0.0005 // 0.5mT Amplitude
ts := (10*1)/f


//External field parameters
Bmax := 450 //Maximum field (mT)
Bmin := 10 //Minimum field (mT)
bs:=1 //Field step 1mT

//Material parameters
Ae:= 1.32e-11 //J/m
Ms:= 4.72e5//4.85e5 //A/m
k1c:= -1.10e4 //J/m^3


// Simulation grid
// World-Size = Nx * Cx
N1 := 180
N2 := 180
N3 := 60
C1 := 3e-9 //in m
C2 := 3e-9 //in m
C3 := 3e-9 //in m
B1 := 0
B2 := 0
B3 := 0
SetMesh(N1,N2,N3,C1,C2,C3,B1,B2,B3)//(Nu
mber of Cells x,y,z; Cell size x,y,z; Repititions
x,y,z)

//Geometry
// Side lengths [m]
s1 := 21e-9
s2 := 21e-9
s3 := 21e-9

// Translation [m]
//+x Direction
px11 := 10e-9
px12 := -14e-9
px13 := 1e-9

px21 := 10e-9
px22 := 14e-9
px23 := 1e-9

px31 := 34e-9
px32 := -1e-9
px33 := 1e-9

px41 := 58e-9
px42 := 2e-9
px43 := 1e-9

px51 := 82e-9
px52 := 4e-9
px53 := 1e-9

px61 := 106e-9
px62 := 6e-9
px63 := 1e-9

px71 := 130e-9
px72 := 8e-9
px73 := 1e-9

px81 := 155e-9
px82 := 4e-9
px83 := 1e-9

px91 := 164e-9
px92 := -20e-9
px93 := 1e-9

px101 := 176e-9
px102 := -44e-9
px103 := 1e-9

//-x Direction
mx11 := -13e-9
mx12 := 4e-9
mx13 := 1e-9

mx21 := -37e-9
mx22 := -2e-9
mx23 := 1e-9

mx31 := -61e-9
mx32 := -4e-9
mx33 := 1e-9

mx41 := -85e-9
mx42 := -14e-9
mx43 := 1e-9

mx51 := -109e-9
mx52 := -4e-9
mx53 := 1e-9

mx61 := -133e-9
mx62 := 1e-9
mx63 := 1e-9

mx71 := -157e-9
mx72 := 10e-9
mx73 := 1e-9

mx81 := -181e-9
mx82 := 14e-9
mx83 := 1e-9

mx91 := -205e-9
mx92 := 20e-9
mx93 := 1e-9

mx101 := -229e-9
mx102 := 24e-9
mx103 := 1e-9

mx111 := -37e-9
mx112 := 22e-9
mx113 := 1e-9
```

Figure 41: Sample script for mumax^3

```
// Simple cubes
cube1 :=
cuboid(s1,s2,s3).transl(px11,px12,px13)
cube2 :=
cuboid(s1,s2,s3).transl(px21,px22,px23)
cube3 :=
cuboid(s1,s2,s3).transl(px31,px32,px33)
cube4 :=
cuboid(s1,s2,s3).transl(px41,px42,px43)
cube5 :=
cuboid(s1,s2,s3).transl(px51,px52,px53)
cube6 :=
cuboid(s1,s2,s3).transl(px61,px62,px63)
cube7 :=
cuboid(s1,s2,s3).transl(px71,px72,px73)
cube8 :=
cuboid(s1,s2,s3).transl(px81,px82,px83)
cube9 :=
cuboid(s1,s2,s3).transl(px91,px92,px93)
cube10 :=
cuboid(s1,s2,s3).transl(px101,px102,px103)
cube11 :=
cuboid(s1,s2,s3).transl(mx11,mx12,mx13)
cube12 :=
cuboid(s1,s2,s3).transl(mx21,mx22,mx23)
cube13 :=
cuboid(s1,s2,s3).transl(mx31,mx32,mx33)
cube14 :=
cuboid(s1,s2,s3).transl(mx41,mx42,mx43)
cube15 :=
cuboid(s1,s2,s3).transl(mx51,mx52,mx53)
cube16 :=
cuboid(s1,s2,s3).transl(mx61,mx62,mx63)
cube17 :=
cuboid(s1,s2,s3).transl(mx71,mx72,mx73)
cube18 :=
cuboid(s1,s2,s3).transl(mx81,mx82,mx83)
cube19 :=
cuboid(s1,s2,s3).transl(mx91,mx92,mx93)
cube20 :=
cuboid(s1,s2,s3).transl(mx101,mx102,mx103)

//Defining material regions
DefRegion(1,cube1)
DefRegion(2,cube2)
DefRegion(3,cube3)
DefRegion(4,cube4)
DefRegion(5,cube5)
DefRegion(6,cube6)
DefRegion(7,cube7)
DefRegion(8,cube8)
DefRegion(9,cube9)
DefRegion(10,cube10)
DefRegion(11,cube11)
DefRegion(12,cube12)
DefRegion(13,cube13)
DefRegion(14,cube14)
DefRegion(15,cube15)
DefRegion(16,cube16)
DefRegion(17,cube17)
DefRegion(18,cube18)
DefRegion(19,cube19)
DefRegion(20,cube20)

// Set geometry and save
chain:=cube1.add(cube2).add(cube3).add(cub
e4).add(cube5).add(cube6).add(cube7).add(cu
be8).add(cube9).add(cube10).add(cube11).ad
d(cube12).add(cube13).add(cube14).add(cube
15).add(cube16).add(cube17).add(cube18).ad
d(cube19).add(cube20)
setgeom(chain)


// Material: Fe3O4
// Parameter
ac11 := vector(1/sqrt(3),-(1/sqrt(2)),1/sqrt(6))
ac12 := vector(1/sqrt(3),(1/sqrt(2)),1/sqrt(6))
Print(ac11)
Print(ac12)
for w:=1; w<=20; w++{
  Msat.SetRegion(w, Ms) //A/m
  Aex.SetRegion(w, Ae) //J/m
  Kc1.SetRegion(w,k1c) //J/m^3
  anisC1.SetRegion(w, ac11)
  anisC2.SetRegion(w, ac12)
  Print(w)
}
alpha = 0.002
gf := 2.12
muB := 9.27400968e-24
hq := 1.054571726e-34
gammaLL = gf*muB/hq


// Storage parameters
OutputFormat = OVF2_TEXT //Text ovf files
tableadd(B_ext)
tableadd(B_eff)
tableadd(B_anis)
tableadd(B_demag)
tableadd(B_exch)
tableadd(B_therm)
tableadd(E_anis)
tableadd(E_demag)
tableadd(E_exch)
tableadd(E_therm)
tableadd(E_total)
tableadd(E_Zeeman)
tableadd(Edens_anis)
tableadd(Edens_demag)
tableadd(Edens_exch)
tableadd(Edens_therm)
tableadd(Edens_total)
tableadd(Edens_Zeeman)
tableadd(ExchCoupling)
tableadd(m_full)
tableadd(maxtorque)
tableadd(LLtorque)
tableadd(torque)
tableadd(STtorque)
tableadd(MaxAngle)
tableadd(spinAngle)
tableadd(geom)
```

Figure 42: Sample script for mumax[3]

```
tableadd(dt)
tableadd(LastErr)
tableadd(NEval)
tableadd(PeakErr)
for q:=0; q<=20; q++{
  tableadd(B_eff.region(q))
  tableadd(B_anis.region(q))
  tableadd(B_demag.region(q))
  tableadd(B_exch.region(q))
  tableadd(Edens_anis.region(q))
  tableadd(Edens_demag.region(q))
  tableadd(Edens_exch.region(q))
  tableadd(Edens_total.region(q))
  tableadd(Edens_Zeeman.region(q))
  tableadd(ExchCoupling.region(q))
  tableadd(m_full.region(q))
  tableadd(LLtorque.region(q))
  tableadd(torque.region(q))
  tableadd(STtorque.region(q))
  tableadd(spinAngle.region(q))
}


// Initial magnetization and relaxation
maxdt=1e-12
DemagAccuracy = 8.0
m=RandomMag()
save(m) // Save m before relaxation
B_ext = vector(bs*450*1e-3, 0,0)
relax()
save(m)
save(B_ext)
save(B_eff)
save(B_anis)
save(B_demag)
save(B_exch)
save(B_therm)
```

Figure 43: Sample script for mumax[3]

A.5. EPR Markers

As described in chapter 3.3, the bacteria have been prepared and washed using different chemicals throughout the sample preparation. The actual spectra show some resonances, which are not to be explained by the presence of magnetite. It can be seen, that in the bulk, as well as in the microresonator spectra of multiple bacteria cells, a resonance appears around $B_{\mathrm{res}} = 318\,\mathrm{mT}$ at $f = 8.9\,\mathrm{GHz}$, corresponding to a g factor of 2. This resonance possibly occurs due to the oxidation of the used buffer chemical HEPES (2-[4-(2-hydroxyethyl)piperazin-1-yl]ethanesulfonic acid), see Figure 44. It has been shown [Gra88], that, if oxidized under the presence of metal ions, the buffer solution shows strong EPR in the observed field range. Broadening in the line for the bulk measurements can be explained by the amount of sample and the possible overlap of single EPR lines due to different molecular orientations inside the resonator and the occuring strayfield of the magnetite particles, resulting in a broadened EPR. Furthermore it can be seen, that the EPR shows slight anisotropic behavior when measured in the bulk measurements, as the line broadens for the in-plane measurements.

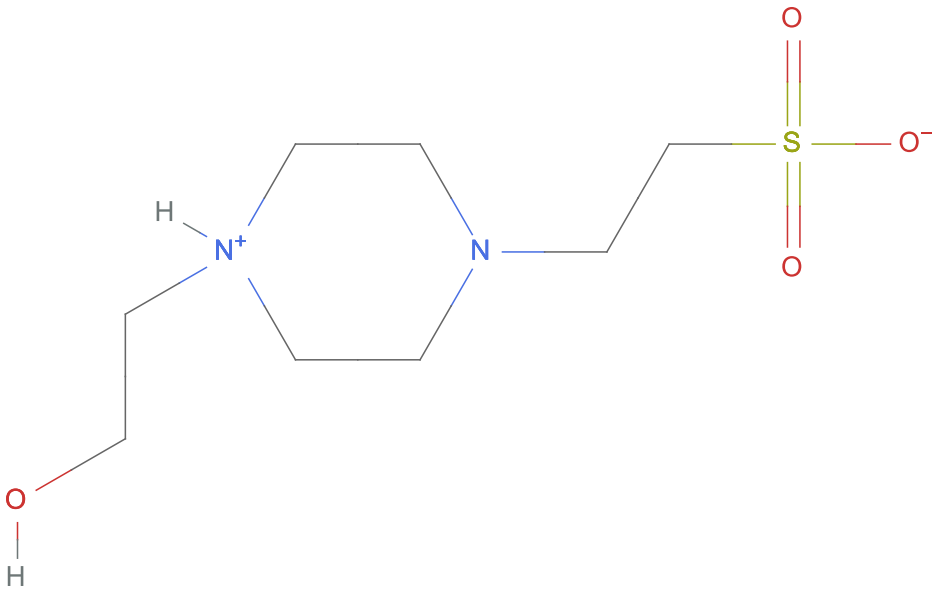

Figure 44: HEPES, molecular structure

List of Tables

List of Figures

References

[Abo13] G. A. Abo, Y. Hong, J. Park, J. Lee, W. Lee, B. Choi. *Definiton of Magnetic Exchange Length.* IEEE Transactions on Magnetics 49(8): 4937 (2013)

[Abr14] L. G. Abraçado, E. Wajnberg, D. M. S. Esquivel, C. N. Keim, K. T. Silva, E. T. S. Moreira, U. Lins, M. Farina. *Ferromagnetic resonance of intact cells and isolated crystals from cultured and uncultured magnetite-producing magnetotactic bacteria.* Physical Biology 11 (2014)

[Aha00] A. Aharoni. *Introduction to the Theory of Ferromagnetism.* Oxford Science Publications (2000)

[And50] P. W. Anderson. *Antiferromagnetism.* Physical Review 79(2): 350 (1950)

[Ban10] A. Banholzer. *Mikroresonatoren zur Messung von ferromagnetischen Strukturen: Herstellung und Charakterisierung.* Diploma thesis, Universität Duisburg-Essen (2010)

[Ban11] A. Banholzer, R. Narkowicz, C. Hassel, R. Meckenstock, S. Stienen, O. Posth, D. Suter, M. Farle, J. Lindner. *Visualization of Spin Dynamics in Single Nanosized Magnetic Elements.* Nanotechnology 22: 295713 (2011)

[Bau13] J. Baumgartner, G. Morin, N. Menguy, T. P. Gonzales, M. Widdrar, J. Cosmidis, D. Faivre. *Magnetotactic bacteria form magnetite from a phosphate-rich ferric hydroxide via nanometric ferric (oxyhydr)oxide intermediates.* Proceedings of the National Academy of Sciences 110(37): 14883 (2013)

[Bel63] S. Bellini. *Su di un particolare comportamento di batteri d'acqua dolce.* , Università di Pavia (1963)

[Bic50] L. R. Bickford. *Ferromagnetic Resonance Absorption in Magnetite Single Crystals*. Physical Review 78(4): 449 (1950)

[Bla75] R. Blakemore. *Magnetotactic bacteria*. Science 190(4212): 377 (1975)

[Bla81] R. P. Blakemore, R. B. Frankel. *Magnetic Navigation in Bacteria*. Scientific American 58–65 (1981)

[Boz03] R. M. Bozorth. *Ferromagnetism*. IEEE Press (2003)

[Bra08] A. Brandlmaier, S. Geprägs, M. Weiler, A. Boger, M. Opel, H. Huebl, C. Bihler, M. S. Brandt, B. Botters, D. Grundler, R. Gross, S. T. B. Goennenwein. *In situ manipulation of magnetic anisotropy in magnetite thin films*. Physical Review B 77: 104445 (2008)

[Chi97] S. Chikazumi. *Physics of Ferromagnetism*. Oxford Science Publications (1997)

[Cor03] R. Cornell, U. Schwertmann. *The Iron Oxides*. Wiley-VHC (2003)

[Don] M. J. Donahue, D. G. Porter. *OOMMF User's Guide, Version 1.0*. Gaithersburg, MD. URL `http://math.nist.gov/oommf/`

[Eat10] G. Eaton, S. Eaton, D. Barr, R. Weber. *Quantitative EPR*. Springer Verlag (2010)

[Fai08a] D. Faivre, N. Menguy, M. Posfai, D. Schüler. *Environmental parameters affect the physical properties of fast-growing magnetosomes*. American Mineralogist 93: 463 (2008)

[Fai08b] D. Faivre, D. Schüler. *Magnetotactic Bacteria and Magnetosomes*. Chemical Review 108: 4875 (2008)

[Fai10] D. Faivre, A. Fischer, I. Garcia-Rubio, G. Mastrogiacomo, A. U. Gehring. *Development of Cellular Magnetic Dipoles in Magnetotactic Bacteria*. Biophysical Journal 99: 1268 (2010)

[Fai15] D. Faivre, T. U. Godec. *From Bacteria to Mollusks: The Principles Underlying the Biomineralization of Iron Oxide Materials.* Angewandte Chemie 127: 4810 (2015)

[Fis08] H. Fischer, G. Mastrogiacomo, J. F. Löffler, R. J. Warthmann, P. G. Weidler, A. U. Gehring. *Ferromagnetic resonance and magnetic characteristics of intact magnetosome chains in Magnetospirillum gryphiswaldense.* Earth and Planetary Science Letters 270: 200 (2008)

[Fri11] N. Friedenberger. *Single Nanoparticle Magnetism: Hysteresis of Monomers, Dimers and Many-Particle Ensembles.* , Universität Duisburg-Essen (2011)

[Geh11a] A. U. Gehring, H. Fischer, M. Charilaou, I. Garcia-Rubio. *Magnetic anisotropy and Verwey transition of magnetosome chains in Magnetospirillum gryphiswaldense.* Geophysical Journal International 187: 1215 (2011)

[Geh11b] A. U. Gehring, J. Kind, M. Charilaou, I. Garcia-Rubio. *The detection of magnetotactic bacteria and magnetofossils by means of magnetic anisotropy The detection of magnetotactic bacteria and magnetofossils by means of magnetic anisotropy.* Earth and Planetary Science Letters 309: 113 (2011)

[Gil04] T. L. Gilbert. *A Phenomenological Theory of Damping in Ferromagnetic Materials.* IEEE Transactions on Magnetics 40(6): 3443 (2004)

[Gra88] J. K. Grady, N. D. Chasteen, D. C. Harris. *Radicals from Good's Buffers.* Analytical Biochemistry 173: 111 (1988)

[Gro14] R. Gross, A. Marx. *Festkörperphysik.* De Gruyter, 2 (2014)

[Han96] M. Hanzlik, M. Winklhofer, N. Petersen. *Spatial arrangement of chains of magnetosomes in magnetotactic bacteria.* Earth and Planetary Science Letters 145: 125 (1996)

[Hei93] B. Heinrich, J. F. Cochran. *Ultrathin Metallic Magnetic Films: Magnetic Anisotropies and Exchange Interactions.* Advances in Physics 42: 523 (1993)

[Hei94] B. Heinrich, J. Bland. *Ultrathin Magnetic Structures II.* Springer-Verlag Berlin Heidelberg (1994)

[Hei07] B. Heinrich. *Exchange Coupling in Magnetic Multilayers*, 227 *Springer Tracts in Modern Physics.* Springer-Verlag Berlin Heidelberg (2007)

[Her06] R. Hergt, S. Dutz, R. Müller, M. Zeisberger. *Magnetic particle hyperthermia: nanoparticle magnetism and materials development for cancer therapy.* Journal of Physics: Condensed Matter 18: S2919 (2006)

[Hey03] U. Heyen, D. Schüler. *Growth and magnetosome formation by microaerophilic Magnetospirillum strains in an oxygen-controlled fermentor.* Applied Microbiology and Biotechnology 61: 536 (2003)

[Ish95] T. Ishii. *Handbook of Microwave Technology.* Academic Press (1995)

[Jen02] H. Jeng, G. Guo. *First-principles investigations of the electronic structure and magnetocrystalline anisotropy in strained magnetite Fe3O4.* Physical Review B 65(094429) (2002)

[K§9] Z. Kąkol, J. Honig. *Influence of deviations from ideal stoichiometry on the anisotropy parameters of magnetite* $Fe_{3(i-\gamma)}0_4$. Physical Review B 40(13): 9090 (1989)

[Kim07] D. Kim, J.Park, K. An, N.-K. Yang, J.-G. Park, T. Hyeon. *Synthesis of Hollow Iron Nanoframes.* Journal of the American Chemical Society 129: 5812 (2007)

[Kit49] C. Kittel. *On the Gyromagnetic Ratio and Spectroscopic Splitting Factor of Ferromagnetic Substances.* Physical Review 76(6): 743 (1949)

[Kit06] C. Kittel. *Einführung in die Festkörperphysik.* Oldenbourg Verlag, 14 (2006)

[Kop06] R. E. Kopp, C. Z. Nah, A. Kobayashi, B. P. Weiss, D. A. Bazylinski, J. L. Kirschvink. *Ferromagnetic resonance spectroscopy for assessment of magnetic anisotropy and magnetostatic interactions: A case study of mutant magnetotactic bacteria.* Journal of Geophysical Research 111(B12S25): 1 (2006)

[Lee15] N. Lee, D. Yoo, D. Ling, M. H. Cho, T. Heyon, J. Cheon. *Iron Oxide Based Nanoparticles for Multimodal Imaging and Magnetoresponsive Therapy.* Chemical Reviews 115: 10637 (2015)

[Lin02] J. Lindner. *Ferromagnetische Resonanz an ultradünnen magnetischen Einfach- und Mehrfachlagen der 3d-Übergangsmetalle – Statik und Dynamik.* Dissertation, Freie Universität Berlin (2002)

[Lin03] J. Lindner, K. Baberschke. *In situ ferromagnetic resonance: an ultimate tool to investigate the coupling in ultrathin magnetic films.* Journal of Physics: Condensed Matter 15: 193 (2003)

[Lin08] J. Lindner, M. Farle. *Magnetic Heterostructures*, 227 *Springer Tracts in Modern Physics*, Magnetic Anisotropy of Heterostructures, 45–96. Springer Verlag (2008)

[Lin10] J. Lindner, C. Hassel, A. V. Trunova, F. M. Römer, S. Stienen, I. Barsukov. *Magnetism of Single-Crystalline Fe Nanostructures.* Journal of Nanoscience and Nanotechnology 10: 6161 (2010)

[Mas15] S. Masur, A. Terwey. *Optimized Microresonators for Ferromagnetic Resonance Measurements on Single Nanoparticles.* Project thesis, Universität Duisburg Essen (2015)

[Mat87] T. Matsunaga, S. Kamiya. *Use of magnetic particles isolated from magnetotactic bacteria for enzyme immobilization Use of magnetic particles isolated from magnetotactic bacteria for enzyme immobilization.* Applied Microbiology and Biotechnology 26: 328 (1987)

[Mat07] T. Matsunaga, T. Suzuki, M. Tanaka, A. Arakaki. *Molecular analysis of magnetotactic bacteria and development of functional bacterial magnetic particles for nano-biotechnology.* Trends in Biotechnology 25(4): 182 (2007)

[Mec97] R. Meckenstock. *Untersuchung der magnetischen Eigenschaften von Fe/Ag-Schichtsystemen mit der konventionellen und der ortsaufgelösten ferromagnetischen Resonanz.* Dissertation, Ruhr-Universität Bochum (1997)

[Mec08] R. Meckenstock. *Microwave spectroscopy based on scanning thermal microscopy: Resolution in the nanometer range.* Review of Scientific Instruments 79: 041101 (2008)

[Mey61] A. J. P. Meyer, G. Asch. *Experimental g' and g Values of Fe, Co, Ni, and their Alloys.* Journal of Applied Physics 32: 330 (1961)

[Nar05] R. Narkowicz, D. S. a, R. Stonies. *Planar microresonators for EPR experiments.* Journal of Magnetic Resonance 175: 275 (2005)

[Nar08] R. Narkowicz, D. Suter, I. Niemeyer. *Scaling of sensitivity and efficiency in planar microresonators for electron spin resonance.* Review of Scientific Instruments 79(084702) (2008)

[Poo83] C. P. Poole. *Electron Spin Resonance: A Comprehensive Treatise on Experimental Techniques.* John Wiley and Sons, Inc. (1983)

[Sch06] A. Scheffel, M. Gruska, D. Faivre, A. Linaroudis, J. M. Plitzko, D. Schüler. *An acidic protein aligns magnetosomes along a filamentous structure in magnetotactic bacteria.* Nature Letters 440: 110 (2006)

[Sch08] D. Schüler. *Genetics and cell biology of magnetosome formation in magnetotactic bacteria.* FEMS Microbiological Review 32: 654 (2008)

[Sch14] C. Schöppner, K. Wagner, S. Stienen, R. meckenstock, M. Farle, R. Narkowicz, D. Suter, J. Lindner. *Angular Dependent Ferromagnetic Resonance Analysis in a Single Micron Sized Cobalt Stripe,.* Journal of Applied Physics 116: 033913 (2014)

[Sin14] A. Singh, S. Sahoo. *Magnetic nanoparticles: a novel platform for cancer theranostics.* Drug Discovery Today 19(4): 474 (2014)

[Sta08] D. D. Stancil, A. Prabhakar. *Spin Waves.* Springer Verlag (2008)

[Stö06] J. Stöhr. *Magnetism - From Fundamentals to Nanoscale Dynamics.* Springer Verlag (2006)

[Suk14] A. Sukhov, P. Horley, J. Berakdar, A. Terwey, R. Meckenstock, M. Farle. *Dipole–Dipole Interaction in Arrays of Fe/FexOy Core/Shell Nanocubes Probed by Ferromagnetic Resonance.* IEEE Transactions on Magnetics 50: 1301209 (2014)

[Ter12] A. Terwey. *Individuelle und kollektive magnetische Resonanz von 43nm Fe/Fe_xO_y Kern/Hülle Nanowürfeln.* Bachelor thesis, Universität Duisburg-Essen (2012)

[Tru08] A. Trunova, R. Meckenstock, I. Barsukov, C. Hassel, O. Margeat, M. Spasova, J. Lindner, M. Farle. *Magnetic characterization of iron nanocubes.* Journal of Applied Physics 104(093904) (2008)

[Van14] A. Vansteenkiste, J. Leliaert, M. Dvornik, M. Helsen, F. Garcia-Sanchez, B. V. Waeyenberge. *The design and verification of MuMax3.* AIP Advances 4: 107133 (2014)

[vG93] O. von Geisau. *Photothermische Untersuchungen der FMR langwelliger kollektiver magnetischer Anregungen in YIG.* , Ruhr-Universität Bochum (1993)

[Von66] S. V. Vonsovskii. *Ferromagnetic Resonance.* Pergamon Press Ltd. (1966)

[Wei04] B. P. Weiss, S. S. Kim, J. L. Kirschvink, R. E. Kopp, M. Sankaran, A. Kobayashi, A. Komeili. *Ferromagnetic resonance and low-temperature magnetic tests for biogenic magnetite.* Earth and Planetary Science Letters 224: 73 (2004)

[Wei07] J. A. Weil, J. R. Bolton. *Electron Paramagnetic Resonance.* Wiley, 2 (2007)

[Zen51] C. Zener. *Interaction between the d-Shells in the Transition Metals. II. Ferromagnetic Compounds of Manganese with Perovskite Structure.* Physical Review 82(3) (1951)

[Zha06] R. Zhan, X. Wang, C. Wu, M. Song, J. L. ad G. Lv, J. Zhou, C. Chen, Y. Dai, F. Gao, D. Fu, X. Li, Z. Guan, B. Chen. *Synergistic enhancement effect of magnetic nanoparticles on anticancer drug accumulation in cancer cells.* Nanotechnology 17: 3622 (2006)

Acknowledgements

Here I would like to thank all those people who helped with this thesis.
First I would like to thank Prof. Dr. M. Farle for the opportunity to write my thesis in this working group.
Special thanks belongs to Dr. R. Meckenstock and Prof. Dr. M. Winklhofer for a good supervision and the fruitful discussions throughout the thesis.
Many thanks to Dr. D. Spoddig who assisted me in the SEM image capturing and with sample preparations at the FIB as well as helpful discussions and help with technical problems.
I want to thank T. Feggeler and C. Derricks for the simulations with mumax^3 and OOMMF.
Thanks to B. Zingsem for the help with Mathematica and the calculations.
I would like to thank Dr. D. Faivre and S. Ghaisari from the Max Planck Institute for Colloids and Interfaces in Golm for the collaboration and the cultivation of the bacteria used in this work.
Dr. M. Wuelling for lending me a micromanipulator unit used for sample preparations.
I want to thank all the colleagues in this workgroup for the nice atmosphere and help throughout the last half year.

Last but not least I want to thank all my loved ones for helping me throughout my studies. Without you I would not have managed to finish.

Versicherung an Eides Statt

Ich versichere an Eides statt durch meine untenstehende Unterschrift,

- dass ich die vorliegende Arbeit - mit Ausnahme der Anleitung durch die Betreuer - selbstständig und ohne fremde Hilfe durchgeführt habe und

- dass ich alle Stellen, die wörtlich oder annähernd wörtlich aus fremden Quellen entnommen sind, entsprechend als Zitate gekennzeichnet habe und

- dass ich ausschliesslich die angegebenen Quellen (Literatur, Internetseiten, sonstige Hilfsmittel) verwendet habe und

- dass ich alle entsprechenden Angaben nach besten Wissen und Gewissen vorgenommen habe,

- dass sie der Wahrheit entsprechen und dass ich nichts verschwiegen habe.

Mir ist bekannt, dass eine falsche Versicherung an Eides Statt nach §156 und nach §163 Abs. 1. des Strafgesetzbuches mit Freiheitsstrafe oder Geldstrafe bestraft wird.

Duisburg, den